Evaluation of cloud and precipitation simulations in CAM6 and AM4 using observations over the Southern Ocean

Xiaoli Zhou[1], Rachel Atlas[1], Isabel L. McCoy[1], Christopher S. Bretherton[1], Charles Bardeen[2], Andrew Gettelman[2], Pu Lin[3], Yi Ming[4]

[1]Department of Atmospheric Sciences, University of Washington, Seattle, Washington, USA

[2]National Center for Atmospheric Research, Boulder, Colorado, USA

[3]Atmospheric and Oceanic Sciences Program, Princeton University, Princeton, New Jersey, USA

[4]NOAA/Geophysical Fluid Dynamics Laboratory, Princeton, New Jersey, USA

Corresponding author: Xiaoli Zhou (Email: xiaoliz@uw.edu)

†Department of Atmospheric Sciences, University of Washington, Box 351640, Seattle, WA 98195-1640

Key points:

1. CAM6 and AM4 simulate observed cloud properties and compositions fairly well within the variability of observations.
2. CAM6 clouds are “too frequent, too bright”; AM4 clouds are “too few, too bright”.
3. Cloud droplet number concentration in CAM6 is typically too low; AM4 clouds include too much small ice and too little snow.

Abstract

This study uses cloud and radiative properties collected from in-situ and remote sensing instruments during two coordinated campaigns over the Southern Ocean between Tasmania and Antarctica in January-February 2018 to evaluate the simulations of clouds and precipitation in nudged-meteorology simulations with the CAM6 and AM4 global climate models sampled at the times and locations of the observations. Fifteen SOCRATES research flights sampled cloud water content, cloud droplet number concentration, and particle size distributions in mixed-phase boundary-layer clouds at temperatures down to -25 C. The six-week CAPRICORN2 research cruise encountered all cloud regimes across the region. Data from vertically-pointing 94 GHz radars deployed was compared with radar-simulator output from both models. Satellite data was compared with simulated top-of-atmosphere (TOA) radiative fluxes.

Both models simulate observed cloud properties fairly well within the variability of observations. Cloud base and top in both models are generally biased low. CAM6 overestimates cloud occurrence and optical thickness while cloud droplet number concentrations are biased low, leading to excessive TOA reflected shortwave radiation. In general, low clouds in CAM6 precipitate at the same frequency but are more homogeneous compared to observations. Deep clouds are better simulated but produce snow too frequently.

AM4 underestimates cloud occurrence but overestimates cloud optical thickness even more than CAM6, causing excessive outgoing longwave radiation fluxes but comparable reflected shortwave radiation. AM4 cloud droplet number concentrations match observations better than CAM6. Precipitating low and deep clouds in AM4 have too little snow. Further investigation of these microphysical biases is needed for both models.

1. Introduction

General circulation models (GCMs) are challenged by uncertainties and biases in the simulation of Southern Ocean clouds, aerosols, and precipitation, and these uncertainties affect simulated global cloud feedback on climate change. The clouds simulated by GCMs participating in the third and fifth Coupled Model Intercomparison Projects (CMIP3 & CMIP5; Meehl et al., 2005) mostly reflected too little sunlight back to space over the Southern Ocean (45º-65ºS) (Trenberth and Fasullo, 2010; Ceppi et al., 2012; Williams et al., 2013). Bodas-Salcedo et al. (2014) and others identified insufficient low cloud cover and insufficient supercooled liquid water in the cold sector

of frontal cyclonic system as likely causes of this bias. Trenberth and Fasullo (2010) suggested that too little low cloud in the current climate might cause an underestimation of positive low cloud feedback on future climate change over this region. Models which glaciate mixed phase clouds at overly warm temperatures also have a spuriously negative high-latitude cloud optical depth feedback, driven by a simulated warming-induced transition from ice-dominated to liquid-dominated low clouds, while satellite observations suggest these clouds are already liquid-dominated (Cordon and Klein 2014; McCoy et al., 2016; Terai et al., 2016; Tan et al., 2016). Improved simulation of Southern Ocean clouds in climate models will help us to better simulate the radiative energy budget in the current climate and to make more reliable future projections of Earth's climate.

Several recent GCM sensitivity studies have shown that the SO cloud bias can be substantially reduced by inhibiting several uncertain stratiform and convective cloud microphysical processes that can glaciate mixed-phase Southern Ocean clouds (Kay et al. 2016, Bodas-Salcedo et al., 2019; Gettelman et al., 2019). This may have led the Coupled Model Intercomparison Project phase 6 (CMIP6) versions of several GCMs (Eyring et al., 2016) with revised treatments of mixed-phase clouds to have more positive global cloud feedback than in their CMIP5 counterparts (Gettelman et al., 2019, Bodas-Salcedo et al., 2019, Zelinka et al., 2020).

Until recently, there were very few in-situ observations available to test and constrain such modeling choices. Satellite observations from active and passive sensors are an invaluable resource, but they have interpretational uncertainties that need to be anchored by in-situ measurements. An evaluation of the CMIP6 GCM simulations of SO

clouds and precipitation based on in-situ observations coordinated with collocated active remote sensing is a key step for future improvement of cloud representations in the models.

Motivated by this, two coordinated field studies were conducted over the sector of the Southern Ocean between Tasmania and the Antarctic sea ice edge in Jan.- Feb. 2018: 1) a U. S. aircraft study based in Hobart, Tasmania, the Southern Ocean Clouds, Radiation, Aerosol Transport Experimental Study (SOCRATES), and 2) an Australian ship-based study, the second Clouds, Aerosols, Precipitation, Radiation, and atmospheric Composition Over the southeRn ocean field study (CAPRICORN2). These two studies used complementary sampling strategies. The research flights targeted weather regimes with low-lying clouds at altitudes below 4 km during daytime, providing detailed multivariate spatial cross-sections through complex cloud fields but no temporal continuity. The ship sampled all weather regimes and times of day, but its only in-situ measurements above the surface were twice-daily radiosondes. Both platforms had vertically-pointing cloud radar and lidar. The data from these two studies pair well because they test different aspects of GCM simulations.

In this paper, we use this data together with satellite measurements to characterize Southern Ocean cloud morphology, cloud and precipitation occurrence and frequency, cloud droplet number concentration (N_d), hydrometeor size distribution, and shortwave (SW) and longwave (LW) radiative effects at the top of atmosphere (TOA). Radiosondes launched on the ship and dropsondes from the aircraft map out the troposphere relative humidity field. We use these uniquely comprehensive observations of cloud and radiative properties to evaluate the atmospheric components of two state-of-the-art CMIP6 GCMs.

The Community Atmosphere Model version 6 (CAM6, Bogenschutz et al., 2018) is the atmospheric component of version 2 of the Community Earth System Model (CESM2), developed by the National Center for Atmospheric Research (NCAR) and many other partners. The Atmosphere Model version 4 (AM4, Zhao et al. 2018) is part of the CM4 climate model (Held et al. 2019) and ESM4 (Dunne et al. 2019) earth system model developed by the Geophysical Fluid Dynamics Laboratory (GFDL).

A centerpiece of our approach for comparing GCMs with observations is the use of nudged-meteorology simulations in which the GCM winds and temperature field are lightly nudged with a 24-hour timescale toward reanalysis, while other simulated fields (e. g. humidity, clouds, aerosols and precipitation) are not nudged and freely evolve. This allows us to focus on model errors in water processes that are probably derived from the local action of physical parameterizations rather than an incorrect synoptic environment.

The models are sampled along the same paths followed by the plane and the ship, so that every observation can be meaningfully compared with model output at the same simulated time and place, without need for compositing or other statistical averaging, similar to Wu et al. (2017) and Bretherton et al. (2019). The nudged-meteorology approach is particularly useful around the rapidly evolving storm systems of the SO.

Recently Gettelman et al. (2020) used SOCRATES and satellite measurements to look at cloud location, cloud phase, and boundary layer structure in CAM6 simulations, and evaluate the improvement of CAM6 simulations compared to CAM5 using monthly averaged satellite retrievals. Our paper complements Gettelman et al., (2020) by assessing cloud and precipitation occurrence and its radiative impacts from a more

140 statistical perspective, and combines unique CAPRICORN2 data and radar simulators for
141 a comprehensive assessment.

142 The remainder of this paper is organized as follows. Section 2 describes our
143 observations and models, including more detail on the nudged-meteorology approach
144 taken here. Section 3 evaluates the representation of low cloud and precipitation in
145 CAM6 and AM4 during the SOCRATES campaign, including cloud and precipitation
146 occurrence and frequency, hydrometeor size distributions, cloud water content and cloud
147 droplet number concentration. Section 4 discusses low and deep clouds in the models
148 during the CAPRICORN2 campaign, using radar data and simulators and satellite-
149 derived TOA radiative fluxes. Section 5 presents conclusions.

150

151 **2. Description of observations, models, and radar simulator**

152 **2.1. SOCRATES measurements**

153

154 During the SOCRATES campaign, 15 research flights of the U. S. National
155 Science Foundation Gulfstream V (GV) research aircraft (EOL 2005) were conducted
156 from Hobart, Tasmania (42ºS, 147ºE) out over the Southern Ocean between 15 January-
157 24 February 2018. The GV aircraft flew roughly southward at its ferry altitude of 6 km to
158 a southernmost waypoint, typically near 58-62°S, chosen to optimize sampling of cold-
159 sector boundary-layer stratocumulus and cumulus. The GV then descended to conduct
160 standardized sampling modules during the generally northbound return legs. Each 45-50
161 minute module, spanning 400-500 km, was made up of 10-minute above-cloud, in-cloud,
162 and below-cloud (150-200 m altitude) legs, and a sawtooth leg consisting of an ascent to

600 m above cloud top, a descent to 150 m above sea surface, and another ascent above the cloud top. A comprehensive suite of instrumentation for sampling mixed-phase cloud, aerosols, and turbulence was deployed (https://www.eol.ucar.edu/content/socrates-aircraft-payload), as well as a vertically-pointing cloud radar and lidar and dropsondes.

The primary in-situ instruments used in the current study are the Vertical-Cavity Surface-Emitting Laser (VCSEL; EOL 2008), the Cloud Droplet Probe (CDP), and the Two-Dimensional Stereo probe (2DS; Wu and McFarquhar, 2019). The VCSEL reported relative humidity (RH), derived as the ratio of measured water vapor concentration and saturated vapor pressure over liquid water at the ambient temperature (per Wexler's formula; Wexler 1976) at a 25 Hz temporal resolution. HARCO heated total air temperature sensors were used for measurement of temperature (T) every 25 Hz.

We use GV remote sensing measurements from the 94 GHz (W-band) HIAPER cloud radar (HCR; EOL 2014) and the high spectral resolution lidar (HSRL; EOL 2010), The radar and HSRL operated at a 2 Hz temporal resolution and could be manually switched to point up or down. The goal was generally to point toward the nearest clouds. Both instruments have a minimum range or 'dead zone' of 150-200 m from the plane, but this was rarely an issue unless the aircraft was flying within a thin cloud layer. Past its dead zone, the HSRL could detect essentially all clouds (with attenuation for thicker clouds), even when the aircraft was flying at its ferry altitude of 6 km. Thus, in this study the combination of the HSRL and the in-situ aircraft cloud probes were used to determine lower-tropospheric cloud occurrence.

The CDP measured liquid water content and cloud droplet size distribution from 1-50 μm at a sampling rate of 10 Hz. The 2DS provided hydrometeor images, from which

data processing software synthesized cloud and precipitation size distributions from 10-1028 μm radius.

2.2: **CAPRICORN2 measurements**

The CAPRICORN2 cruise of Australia's Research Vessel (RV) *Investigator* spanned Jan. 10-Feb. 21, 2018. It was a sequel to earlier voyages in 20-29 March 2015, and March-April 2016 described in Protat et al., 2017 and Mace et al. 2018. We use radar reflectivity profiles collected by an onboard calibrated 95 GHz W-band vertically pointing cloud radar (see Mace et al. 2018 for more details). The radar reflectivity has been corrected for wet radome attenuation. We also use twice-daily radiosondes from the cruise.

2.3 Satellite measurements

To assess the GCM-simulated top-of-atmosphere (TOA) radiative fluxes, we use edition 4A of National Aeronautics and Space Administration (NASA) Clouds and the Earth's Radiant Energy System (CERES; Wielicki et al., 1996) synoptic (SYN) cloud and radiation products (Doelling et al., 2013; Rutan et al., 2015). We use the hourly TOA fluxes of reflected shortwave radiation (RSW) and outgoing longwave radiation (OLR). The CERES SYN data is available on a 1^{o}x1^{o} grid (https://ceres.larc.nasa.gov/products.php?product=SYN1deg). We extract the nearest grid points to the contemporaneous aircraft and ship locations for comparison with models.

2.4 **CAM6 model description**

CAM6 was comprehensively described in Bogenschutz et al., (2018) and Gettelman et al. (2019). This section summarizes key features of CAM6 for this study. CAM6 implements the Cloud Layers Unified by Bi-normals (CLUBB, Golaz et al. (2002), Larson et al. (2002)) parameterization to replace the planetary boundary layer, shallow convection, and cloud macrophysical parameterization schemes used in CAM5. The unified CLUBB scheme bypasses the complexity of interactions between schemes to improve performance for the simulation of boundary layer clouds, especially of intermediate types of regimes such as the stratocumulus to cumulus transition (Bogenschutz et al., 2013; Guo et al., 2015). CAM6 retains the deep convection scheme of Zhang and McFarlane (1995) used in CAM4 and CAM5. The precipitation from the CLUBB and deep convection schemes is referred as large-scale (stratiform) and convective precipitation respectively. CLUBB diagnoses cloud fraction and cloud liquid water from a joint double-Gaussian probability density function (PDF). Ice and liquid cloud fractions in CLUBB are the same and are analytically diagnosed by integrating over saturated portions of the joint PDF (Guo et al., 2014). The total cloud fraction in CAM6 combines CLUBB and deep convective cloud cover fractions, and an ice cloud fraction assuming maximum overlap.

The CAM6 microphysics package incorporates a two-moment scheme for 4 classes (liquid, ice, and large scale rain and snow) with updated ice nucleation parameterization, MG2 (Gettelman and Morrison, 2015). MG2 is coupled to a physically based mixed phase ice nucleation scheme (Hoose et al 2010) implemented in CAM6 with modifications for a PDF of contact angle by Wang et al (2014). MG2 accounts for preexisting ice during cirrus ice nucleation (Shi et al 2015).

Aerosols are predicted by a four-mode version of the Modal Aerosol Module (MAM4) (Liu et al., 2016), initialized based on climatological profiles in year 2000 from CMIP6 emissions inventory. The activation of aerosols into cloud droplets in CAM6 is diagnosed as a function of the modeled sub-grid scale updraft velocity and aerosol compositions and size distribution (Abdul-Razzak and Ghan 2000).

The CAM6 simulations in this paper are run with prescribed sea surface temperature. A Finite-Volume (FV) dynamical core of 0.9º longitude x 1.25º latitude resolution is used with 32 vertical levels and a model time step of 30 minutes. To facilitate model evaluation against observations, CAM6 was run in a nudged configuration (Lamarque, 2011) using the NASA Modern-Era Retrospective analysis for Research and Applications version 2 (MERRA-2; Rienecker et al., 2011; Molod et al., 2015) horizontal winds, temperature, and monthly mean sea surface temperature (SST) with a relaxation timescale of 24 hours. MERRA-2 nudging fields are interpolated to the CAM6 vertical levels before nudging. The CAM6 simulation is performed starting on January 1st 2017, to ensure proper spin-up of aerosol and land-surface fields well before any observational comparisons. Model outputs along the tracks of the aircraft and ship (specifically, from the nearest model grid points to the current ship and aircraft locations) are calculated in-line and output at time steps of 1 minute and 10 minutes respectively.

2.5 AM4 model description

AM4 was comprehensively described by Zhao et al. (2018). Here we summarize those physical parameterizations from the model that are particularly relevant to its simulation of Southern Ocean clouds and aerosols. AM4 uses a double plume shallow

convection scheme adapted from Bretherton et al., (2004), and a deep convection scheme based on a cloud work function relaxation closure (Zhao et al., 2018). The macrophysical scheme of large-scale clouds in AM4 follows Tiedtke (1993). Cloud water content and fractional cloud cover are described prognostically by large-scale budget equations. The increase in cloud cover is determined by the fraction of the cloud-free area exceeding saturation. AM4 implements a one-moment microphysics scheme for liquid water following Rotstayn (1977) and Rotstayn et al., (2000) with an inclusion of a prognostic scheme for cloud droplet number concentration (Ming et al., 2007), as in AM3. A rain profile is diagnosed at each time from the cloud properties (Rotstayn et al., 1997).

Ice is predicted from water vapor diffusion at the expense of liquid water (the Wegener-Bergeron-Findeisen process) and homogeneous freezing of liquid water at temperatures colder than -40ºC. Ice melts to form liquid water at temperatures warmer than 0ºC. In AM4, there is no distinction between falling ice, snowflakes and graupel. All forms of atmospheric ice are represented by a single variable. The ice particles fall with a mass-weighted mean velocity calculated assuming fall speed is proportional to the 0.16 power of particle diameter. Falling ice particles are approximated by a negative exponential distribution with effective radius determined by temperature that ranges from 15 – 100 μm (Donner et al., 1997).

Aerosols in AM4 are predicted based on climatological sources in year 2016 from the CMIP6 emissions inventory; only the mass is prognosed for each aerosol type with a fixed assumed size distribution (Zhao et al., 2018). The activation of aerosols into droplets uses the parameterization of Ming et al. (2006).

AM4 uses the GFDL Finite-Volume Cubed-Sphere dynamical core (FV^3; Harris and Lin, 2013; Putman and Lin, 2007) with a grid of approximately 100 km horizontal resolution and 33 vertical levels. For the simulations presented here, AM4 was run in a nudged configuration (Jeuken et al., 1996) similar to that used for CAM6, with the same 24 hour nudging timescale, but instead nudged to the fifth generation of the European Centre for Medium-Range Weather Forecasts (ECMWF) atmospheric reanalysis of the global climate (ERA5; Hersbach and Dee, 2016) horizontal winds, temperature, and surface pressure with a relaxation time of 24 hours. Like CAM6, the AM4 simulation starts on January 1st 2017. Data is output every 3 hours for radiation fields and 1 hour for other quantities. The nearest model grid points to the ship and aircraft locations were extracted from the AM4 simulations by linearly interpolating to the observation point for comparison with observations and CAM6.

2.7 COSP radar simulator

Within each grid column, the profiles of cloud and precipitation are converted to profiles of synthetic radar reflectivity using implementations of the Cloud Feedback Model Intercomparison Project (CFMIP) Observation Simulator Package (COSP; Bodas-Salcedo et al., 2011) in the two GCMs. CAM6 and AM4 use COSP version 2.1 and 1.4.1 respectively (Bodas-Salcedo et al., 2011; Swales et al., 2018), but there is no crucial scientific difference between COSP versions. In this study, we focus on use of the CloudSat simulator within COSP. It provides synthetic radar reflectivity at a frequency of 94 GHz and can be compared with the observed W-band reflectivity.

The implementation of COSP in a GCM usually makes some additional model-specific assumptions that are not part of the GCM, are not necessarily well documented, and which may impact the synthetic radar reflectivity. For example, the hydrometeor size distribution assumptions can be slightly different between COSP and the parent GCM microphysics scheme. In the CAM6 COSP, all hydrometeors are described with modified gamma distributions. In the CAM6 microphysics scheme, cloud drops are described with a gamma distribution while ice, rain, and snow are assumed to have exponential distributions (gamma with m=0).

The AM4 microphysics scheme has a single ice category that includes both cloud ice and snow and has an aggregate fall speed. In this sense, snow is simply falling ice. AM4 treats the total ice and snow concentration as cloud ice in COSP, which is assigned to have the temperature-determined effective radii of cloud ice particles in AM4. Furthermore, the clear-sky ice flux (flux of ice outside of cloud entering the unsaturated portion of the grid box from above) is used for snow in COSP with effective radii computed internally in COSP. Snow inside clouds is not accounted for explicitly. The impact on the synthetic radar reflectivity of these differences in the assumptions made between COSP and the GCM microphysics scheme is discussed in Appendix B.

The COSP interface varies between host models. CAM6 uses COSP's default -column generator to produce 10 homogenous sub-columns, while AM4 treats the sub-grid cloud and precipitation fields from the radiation scheme as the COSP sub-columns, rather than using the default COSP sub-column generator. We observed little difference between the sub-columns. The insufficient sub-column variability in COSP's default sub-

column generator may lead to overestimated radar reflectivity and probability of precipitation compared to the satellite observations (Song et al., 2018).

3. Low clouds and precipitation in CAM6 and AM4 simulations during SOCRATES

In this section, we will use in-situ and remote sensing observations from SOCRATES to evaluate the macrophysical and microphysical properties of clouds and precipitation in CAM6 and AM4. SOCRATES sampling focused on low clouds with cloud top height lower than 4 km and little or no precipitation falling from any overlying clouds through the 4 km level. We select RF09 (a case of cumulus rising into stratocumulus) and RF12 (a stratocumulus case) as two examples to demonstrate single-flight comparisons of observations and GCM simulations of shallow cumulus and stratocumulus regions, followed by cloud-related statistics across the whole campaign.

3.1 RF09 temperature, relative humidity, cloud and precipitation comparisons

Fig. 1 shows time-height plots of T, RH, in-cloud cloud water content (CWC), and precipitating particle number density (NLarge, described below) along Flight RF09 (inside the black channel) overlying the corresponding fields simulated by CAM6 and AM4 respectively. The microphysical fields are only plotted over the 0-4 km altitude range to highlight low clouds and their environment, while the thermodynamic fields are

plotted from 0-8 km altitude to encompass the ferry leg and provide synoptic-scale context.

RF09 targeted an extensive deck of cold, low-level cloud in the cold sector of a mid-latitude cyclone south and east of Tasmania. Two sampling modules were completed in the cold sector regions south of 50ºS. As seen in Figs. 1a and 1e, the boundary-layer cloud tops, at a height of 2.5 km, have a cloud top temperature near -15ºC. The temperature in the two nudged GCM simulations agrees with the in-situ observations to within 1-2 C. Since temperature is a nudged field, this indicates that the nudged-meteorology approach is working as hoped.

Relative humidity (Fig. 1b) is important for producing clouds. It is a more challenging test for the nudged GCM simulations, since their humidity fields are not constrained with reanalysis data. For both observations and models, the RH in this paper is computed based on liquid saturation. In RF09, the high-RH boundary layer is capped by dry, low-RH, subsiding air above 2.5 km. The free-tropospheric RH is fairly well simulated by both models. Inside the boundary layer, the observed RH is horizontally variable, and is relatively low in the ascent portion of a cloud-free sawtooth near 57ºS in the return leg of RF09. This is suggestive of shallow cumulus rising into a broken stratocumulus layer, a common cold-sector cloud type. As seen in Figs. 1b and 1c, both models capture the boundary layer depth qualitatively well except that they underestimate RH at the top of the boundary layer. The boundary-layer RH in CAM6 is comparable to observations (Fig. 1b), but the AM4 boundary layer is drier than observed (Fig. 1c).

Figs. 1c and 1g show the observed and modeled in-cloud water content (CWC) during RF09. This is an even more challenging comparison for the models because it

requires the models to have both accurate cloud placement and cloud microphysics. The observed CWC is taken from the GV CDP and is plotted when its value exceeds 0.01 g m^{-3}. CWC less than 0.01 g m^{-3} is masked in gray. For the GCMs, the cloud-containing grid cells are distinguished from clear-sky grid cells by having nonzero cloud water mixing ratio and the in-cloud water content is calculated by dividing grid-mean cloud water content by simulated cloud fraction. To be consistent with observations, the GCM CWC is plotted when its value exceeds 0.01 g m^{-3}.

To shed light on the representation of precipitation in the GCMs, we compute in-cloud NLarge (Fig. 1d). NLarge is computed from 2DS particle size distributions (PSD) as the concentration of large precipitating particles with radius greater than 100 microns. The observed NLarge is compared against the CAM6 counterpart along the flight track computed in the same way as in observations based on the model PSD of fraction mean cloud and precipitation. The `fraction-mean' cloud and precipitation are calculated by dividing grid-mean cloud and precipitation quantities by simulated cloud and precipitation fraction respectively. The CAM6 precipitation fraction is set to be the same as the cloud fraction in each cloud-containing grid cell and to the cloud fraction of the lowest cloud-containing grid cell below cloud. Because precipitation in AM4 is treated diagnostically, NLarge is not computed by AM4.

The RF09 sawtooth legs sampled a broken cloud field with intermittent CWC (Fig. 1c). CAM6 generally underestimates its cloud water content (Fig. 1c) but overestimates NLarge (Fig. 1d). The CWC in AM4 in RF09 agrees better with observations than CAM6, but the AM4 clouds have lower cloud base heights compared to observations, a bias seen in many cases during the SOCRATES campaign.

3.2 RF12 temperature, relative humidity, cloud and precipitation comparisons

Fig. 2 compares observations and simulations for an extensive stratocumulus case sampled during RF12 in two modules south of 55ºS. The stratocumulus deck topped a fairly well-mixed 1500 m deep boundary layer, with a cloud top temperature around -9ºC capped by a 5ºC temperature inversion. The cloud deck was in the cold sector of a weak cyclone. Figs. 2a and 2b confirm that the temperature in the nudged models is consistent with the observations for RF12, like in RF09. Both CAM6 and AM4 clearly show low RH at the top of the boundary layer, suggesting biased low boundary layers in these GCMs. As one might expect, the CAM6 CWC and NLarge in the comparatively horizontally homogeneous stratocumulus decks of RF12 agree better with observations than these quantities in the more heterogeneous cumulus regions of RF09. However, CAM6 also tends to miss the light precipitation and spatially intermittent snow that formed in the thicker centers of mesoscale closed cells during RF12 (e.g., -58ºN and -56ºN in the return flight in Fig. 2d). CAM6 and especially AM4 simulate a cloud base height that is too low compared to the approximately 1 km base observed in RF12 (Figs. 2c and 2g). In AM4, the simulated clouds extend down to the ground level.

3.3 Statistical all-flight comparisons of temperature, relative humidity, cloud and precipitation

In order to test the accuracy of the large-scale meteorology in the GCMs, the root mean square (RMS) error was calculated between the observations and GCMs. Across all campaign flights, observed temperature and humidity along the flight track were

413 averaged over 50 m bins in altitude during each 2 minute time interval. The two nudged
414 GCMs were similarly sampled. CAM6 and AM4 had RMS temperature errors of 1.3 K
415 and 1.4 K, remarkably small considering the remote sampling region and large synoptic
416 variability. This is mostly a testament to the accuracy of the reanalysis to which the
417 GCMs were being nudged (which match the observations within even smaller RMS
418 errors of less than 1 K). However, it also shows both GCMs are very good short-term
419 weather forecast models that are able to retain this level of accuracy for at least a day (the
420 nudging timescale).

421 Humidity is highly variable and was not nudged, so it is a much more challenging
422 comparison for the models. We use RH as a measure of humidity, since it has
423 comparable variability across RMS errors across the whole range of sampled heights.
424 Across all flight samples, the RMS error of RH is 23% and 22% for CAM6 and AM4
425 respectively. For comparison, the ERA5 and MERRA-2 reanalysis had slightly smaller
426 RMS RH errors of 17% and 19%. Such errors are large enough to affect the existence
427 and placement of cloud layers, even in a GCM with perfect microphysics.

428 Cloud placement errors reduce the value of a point-by-point comparison of GCM
429 vs. observed cloud properties. It is more illuminating to make a statistical comparison of
430 mean biases in GCM vs the observed CWC at the same overall region, altitude range, and
431 time. We bin the observed and simulated CWC for the 15 SOCRATES flights into boxes
432 of 500 m in altitude and 25 minutes (equivalent to 210 km at a typical flight speed of 140
433 m s^{-1}) in time along the flight track. This binning box is chosen to be big enough to
434 reduce sampling noise but small enough to still represent the local CWC. Boxes in which
435 the binned average CWC < 0.01 g m^{-3} for either the models or the observations are

436 excluded from the statistics. Boxes with less than ten observed samples are screened out.
437 This leaves 133 binned samples, most of which are in altitudes below 3 km. Fig. 3
438 presents the bin-mean and range of CWC over all time bins within each altitude band.
439 The model and observed CWC interquartile ranges generally agree with each other
440 between 1.5~2 km (although with large spread). CWC is clearly overestimated, especially
441 by AM4, below 1 km, an indication that the simulated cloud base is systematically too
442 low as in the RF09 and RF12 examples. On the other hand, in-cloud CWC for both
443 GCMs, especially AM4, is biased low above 2.5 km compared to observations,
444 suggesting that the GCM clouds tend to have a slightly lower cloud top height. This is
445 consistent with the low RH bias at the top of the boundary layer seen for RF12 in Figs. 2b
446 (CAM6) and more prominently in Fig. 2f (AM4).
447
448 **3.4 Low cloud occurrence**
449 Occurrence of low clouds with tops below 4 km in CAM6 and AM4 columns cannot
450 be evaluated using the in-situ observations, since they targeted cloud layers. Instead, it is
451 evaluated in this section using a column cloud fraction based on combining a HSRL
452 backscatter threshold to detect cloud above or below the aircraft and the GV CDP liquid
453 water content to detect cloud at the aircraft level which may not extend outside the 150 m
454 lidar dead zone, or which may attenuate the lidar beam before it reaches the cloud edges.
455 Within a lidar sampling time of 0.5 s, low cloud is flagged if any of the 10 Hz CDP liquid
456 water content measurements exceeds 10^{-4} kg m^{-3} below 4 km, or if the maximum HSRL
457 backscatter below 4 km altitude exceeds a threshold of $3x10^{-5}$ m^{-1} sr^{-1}. This backscatter

458 threshold effectively separates cloud echoes from those of aerosols, as documented in
459 Appendix A.

460 Examples of the lidar backscatter for RF09 and RF12 are shown in Figs. 4a and 4e,
461 where cloud boundaries (i.e., cloud tops when the aircraft was above and cloud bases
462 when below) are well captured by HSRL as seen from the strong lidar backscatter near 1
463 to 2 km. The observed upper cloud boundaries (cloud tops) are slightly higher than those
464 implied by the GCM cloud fraction maps.

465 We define the observed low cloud fraction as the fraction of low cloud flags during
466 every 10 minutes (equivalent to ~1 degree at a typical flight speed of 200 m s^{-1}). We
467 compare this with the corresponding low cloud fraction averaged over the same time
468 periods when there is observational data in CAM6 and AM4 (e.g., Figs., 4b, c, f, and g).
469 The low cloud fraction for each GCM is computed following that GCM's vertical cloud
470 overlap assumptions (maximum-random overlap for CAM6 and exponentially decaying
471 overlap for AM2 with a length scale of 2 km (Zhao et al., 2018)). The regions outside of
472 the HSRL view zone (i.e., regions above/below the aircraft when the HSRL pointed
473 down/up) are masked out before computing GCM low cloud fraction (grey shading in
474 Fig. 4).

475 The low cloud fraction comparisons for RF09 and RF12 are shown in Figs. 4d and
476 4h. As suggested by the lidar backscatter profiles in Fig. 4a and 4e, the observed low
477 cloud fraction in the cumulus regions in RF09 is smaller than that in the stratocumulus
478 regions in RF12. In both flights, CAM6 typically simulates a low cloud fraction that is
479 too large, whereas that in AM4 is too small.

Similar low cloud fraction biases are present across the 15 SOCRATES flights. Fig. 5a shows an all-flight histogram of 10-minute average low cloud fraction. Low clouds, either alone or co-occurring with cloud layers aloft, are observed in 96% of the 10-minute intervals during SOCRATES. About half of the intervals have a low cloud fraction greater than 80%. Only ~10% of the intervals have a low cloud fraction less than 20%. In CAM6, intervals of nearly complete low cloud cover (greater than 90%) occur 60% of the time vs. ~30% of the time in AM4 and 45% in the observations. Over half of the intervals including low clouds in AM4 are characterized by a low cloud fraction smaller than 50%, about twice as frequent as CAM6 and observations.

Another way to present this data is by binning the 10-minute intervals by the observed low cloud fraction, and testing how well the models replicate the low cloud fraction within each bin (Fig. 5b). Ideally, a model would lie on the 1:1 line with no scatter about the observations in this box-whisker plot, but from our other comparisons we expect both large scatter (a large interquartile range of simulated cloud fraction for a given observed cloud fraction) and bias. Indeed, the scatter is large, and the interquartile ranges show that in most bins, about 75% of the CAM6 samples lie above the observed cloud fraction, while about 60% of the AM4 samples lie below the observed cloud fraction. One exception for AM4 is that it produces too much cloud when the observed cloud fraction is less than 10%. This could be due to geographical misplacement of scattered cloud rather than parameterization biases given its agreement with observations for the 10-20% low cloud fraction bin. In summary, CAM6 overestimates and AM4 underestimates low cloud fraction in the cold-sector low cloud regimes sampled by SOCRATES.

3.5 TOA upwelling SW and OLR

Biases in CWC and low cloud fraction contributes to radiative biases in the GCMs. A conventional way to evaluate the impact of cloud on radiation is to compute cloud radiative forcing, defined as the difference of net downward radiative fluxes at TOA with and without cloud. However, since the retrieval of clear-sky radiation from satellite observations inevitably involves uncertainty, in this study we instead compare observed and simulated TOA reflected shortwave and outgoing longwave radiative fluxes as more reliably observed proxies for cloud effects on radiation. We recognize that they may also incorporate biases not related to cloud, e. g. in humidity or surface properties. The radiative flux estimates are matched to the same locations and times as the low cloud fraction estimates.

Fig. 6 shows the TOA RSW and OLR fluxes along the flight tracks from CERES SYN (Section 2.3) and from the two models, binned by observed low cloud fraction. Consistent with the overestimated cloud fraction in CAM6, the RSW in CAM6 is biased high for all bins of observed low cloud fraction. This high bias remains significant even when the observed low cloud fraction is 90-100%, suggesting that the low clouds in CAM6 are not only too frequent, but also too bright. As a result, the average RSW in CAM6 over the entire SOCRATES field campaign is about 20% higher than observed. The overestimate of low cloud cover in CAM6 also leads to underestimated OLR in bins with 50% or less observed low cloud cover. Since the CAM6 cloud tops are at altitudes comparable to observed, although slightly low-biased, they appear not to have large cloud-top temperature biases. Thus, when the observed and CAM6 cloud fractions are

near to 100%, the average OLR of CAM6 is similar to observed. The radiation bias of CAM6 ('too frequent, too bright') is consistent with the climatological cloud radiative effect shown in Gettelman et al. (2020).

In contrast, the underestimated low cloud fraction in AM4 allows for more OLR originating from the sea surface to escape to space, contributing to a sizable high OLR bias in all cloud fraction bins. Surprisingly, the AM4 TOA upwelling SW is comparable to observations in all observed cloud fraction bins. This implies the clouds are optically thicker than observed, i. e. AM4 has a 'too few, too bright' bias for SO low clouds, which is common in CMIP5 models (Nam et al., 2012; Engstrom et al., 2015).

3.6 Microphysics in precipitating and non-precipitating low clouds

We now investigate some underlying model-observation discrepancies in microphysics that may contribute to the radiation biases in models associated with Southern Ocean low clouds.

We quantify the occurrence of precipitating and non-precipitating low clouds in observations and CAM6 along the flight track sorted by ambient temperature (Fig. 7a). An observed or CAM6 low cloud is classified as precipitating if NLarge (defined in Section 3.1 as the concentration of cloud particles with radius bigger than 100 μm; recall also that this cannot be computed for the simpler AM4 microphysics) is greater than 1 x 10^{-4} m^{-3} in observations or CAM6 simulations. The occurrence is computed in cloud regions where CDP CWC exceeds 0.01 g m^{-3}. Eighty-five percent of the SOCRATES samples were collected in cold clouds (at temperatures below freezing), of which only ~10% were precipitating. This is partly because the GV intentionally avoided long flight

549 legs in drizzling supercooled clouds for safety. Repeating the analysis based on the
550 nearest CAM6 grid cells along all 15 SOCRATES flight tracks (Fig. 7b), we find that the
551 CAM6 clouds span a generally similar temperature with comparable precipitation
552 occurrence, although precipitation occurrence in CAM6 clouds does not agree that well
553 with observed clouds during individual flights (e.g., precipitation is overestimated in
554 RF09 but underestimated in RF12 in CAM6; Figs. 1d and 2d). The imperfect match
555 during individual flights might be because the deficient representation of the cloud
556 intermittency in CAM6.

557 We compared the hydrometeor size distributions observed from the CDP and 2DS
558 averaged over the nonprecipitating and precipitating clouds with those inferred along the
559 flight tracks from CAM6 (Fig. 8), summed over cloud, rain, ice and snow. As seen in Fig.
560 8a, nonprecipitating clouds display a unimodal distribution with a peak around 10 μm
561 radius. This unimodal distribution is well represented in CAM6 and is dominated by
562 liquid. CAM6 underestimates the number of cloud droplets with radii less than 20 μm,
563 which dominate the overall cloud droplet number concentration. This bias is larger for the
564 precipitating clouds (Fig. 8b).

565 By definition, the observed number of particles with radius > 50 μm is larger for
566 precipitating clouds, leading to a shoulder in the observed droplet size distribution seen in
567 Fig. 8b. The CAM6 simulations have a comparable increase in rain (blue dash) at 50-300
568 μm radii and in snow (red dash) at radii exceeding 300 μm, suggesting that there is
569 slightly more snow on average in CAM6 than in observations. The model PSDs should
570 not be expected to agree perfectly well with observations on the large-radius tail, given a
571 simple bulk two-moment scheme in CAM6. Note that the PSD in this study is computed

572 from in-cloud legs defined as CWC > 0.01 g m^{-3}. CAM6 is found to have more rain than
573 observations if a less strict in-cloud threshold is used (Gettelman et al., 2020).
574
575 **3.7 Phase partitioning**
576 The supercooled boundary-layer clouds sampled by the GV at temperatures of -5
577 to -25ºC were a mix of small liquid drops that dominate the cloud optical depth and
578 (when precipitating) larger ice and snow particles. This conclusion is based on several
579 complementary lines of evidence.
580 We visually inspected representative images from the 2DS and the PHIPS HALO
581 (Schnaiter, 2018), a new imaging instrument deployed on the GV for SOCRATES that is
582 optimized to detect ice particles with radii between 20-300 μm and liquid drops with radii
583 of 60-300 μm (Abdelmotaleb et al., 2016; Schnaiter et al., 2018). These images suggest
584 that in the precipitating boundary-layer clouds sampled by the GV at temperatures of -5
585 to -25ºC, most of the larger particles (radius > 100 μm) are aspherical frozen
586 hydrometeors.
587 The SOCRATES 2DS data have insufficient spatial resolution to clearly
588 discriminate the phase of small particles with radii less than 100 μm. We instead used a
589 comparison between the liquid water content inferred from the CDP and from a CSIRO
590 (The Commonwealth Scientific and Industrial Research Organization) King hotwire
591 probe to test for the presence of small ice particles of radius less than 25 um, the size
592 range dominating the cloud droplet number concentration and thus optical depth. Such
593 particles would be detected by the CDP but the data processing algorithm would treat
594 them as liquid water droplets, which introduces a high bias in CDP-inferred cloud water

595 content due to their lower density. Small ice particles should affect the CSIRO King
596 probe's LWC measurement rather differently. For instance, ice might partly bounce off
597 the hot wire causing the King probe to underestimate the cloud ice contribution to the
598 cloud water content. Hence a comparison of the LWC inferred from the two instruments
599 can test the presence of cloud ice. Fig. 9 shows a two-dimensional histogram of the two
600 LWC measurements over all SOCRATES low cloud sampling at temperatures -5 to -
601 25ºC, presented as a two-dimensional histogram. The strong concentration of data along
602 the 1:1 line is evidence that small particles (radius < 25 um) are predominantly
603 supercooled liquid droplets.

604 Mace et al., 2018 reports that the light scattering from supercooled Southern
605 Ocean boundary layer stratocumulus clouds mostly comes from liquid droplets, based on
606 an analysis of ship-borne lidar depolarization ratios during CAPRICORN. Our visual
607 inspection of plots of HSRL depolarization ratios from boundary-layer cloud tops
608 observed during SOCRATES supports this conclusion.

609 The hydrometeor PSDs in CAM6 (Fig. 8) are also dominated by supercooled
610 liquid droplets at small sizes.

611

612 **3.8 Cloud droplet number concentration (N_d)**

613 We compare observed in-cloud N_d, computed as the summation of cloud droplets
614 measured by the CDP when the CDP CWC > 0.01 g m^{-3}, with the GCM-simulated in-
615 cloud N_d. Fig. 10 shows the RF09 and RF12 examples. AM4 N_d is comparable to
616 observations, but CAM6 significantly underestimates N_d.

These flights are representative of SOCRATES as a whole. Fig. 11 shows interquartile range boxes of observed and GCM in-cloud N_d measured across all 15 SOCRATES flights and binned similarly to the in-cloud CWC described in Section 3.1. Points where binned average N_d <1 cm^{-3} for either the models or the observations are excluded from the statistics. Fig. 11 shows that the observed N_d clusters around 25-150 cm^{-3} with the highest N_d (> 100 cm^{-3}) occurring mostly near 0.5-1.5 km. CAM6 shows a low bias in N_d above 500 m which amplifies with height. AM4 simulates more high N_d outliers than observed for clouds above 2 km, and does not simulate the relatively uncommon occurrences of observed N_d lower than 40 cm^{-3}. On average, however, AM4 produces a mean N_d at all altitudes much closer to observations than CAM6.

CAM6's low N_d bias could be due to insufficient CCN production or too small a fraction of aerosol activated in the model. McCoy et al., (2020b, in prep) finds that CAM6 simulates CCN concentrations fairly well during SOCRATES with no significant low bias. We find that there is no significant statistical bias in precipitation scavenging of CCN in CAM6 when all cases are considered. Atlas et al. (2020) finds CAM6 simulates too little cloud-layer turbulence in stable and neutral boundary layers, which could lead to an under activation of CCN. However, CAM6 *also* underestimates N_d in unstable boundary layers for which its simulated turbulence is on average consistent with observations. This suggest that there may be multiple competing biases in the model. Disentangling these compounding influences will be necessary to understand the cause of N_d bias in CAM6 and should be the topic of future investigations.

4. Clouds and precipitation in CAM6 and AM4 simulations during the CAPRICORN2 campaign

The upward-pointing 94 GHz shipborne radar deployed on the *R/V Investigator* during CAPRICORN2 sampled whatever clouds were overhead, including many periods of deep clouds with cloud tops above 4 km that were not targeted in SOCRATES. We use this unique radar dataset to evaluate the representation of both deep and low clouds in the GCMs.

4.1 Relative humidity, cloud morphology, and TOA radiative fluxes

We use the 1-15 February, 2018 period of the CAPRICORN2 campaign to illustrate typical model biases. Fig.12a shows a time-height section of radar reflectivity during this period. Low clouds with cloud tops below 4 km were regularly observed while deep cloud layers reaching above 6 km were also frequent. The deep clouds are often associated with significant precipitation indicated by strong reflectivity (>0 dBZ) near the surface, which also often attenuates the W-band radar echo below detectability above 6 km. The precipitation from the thin low clouds is much weaker. As one would expect, the cloudy, precipitating regions are collocated with high relative humidity in a time-height section created from the twice-daily ship-launched radiosondes (Fig. 12b). The RH (computed based on liquid saturation) is shown in Fig. 10c and 10d for CAM6 and AM4. Both models qualitatively reproduce the RH profiles for low cloud regimes sampled along the ship track. CAM6 slightly overestimates the observed RH in regions of deep cloud while AM4 substantially underestimates RH in those regions and also

661 simulates a shallower cloudy boundary layer than observed, as we also saw in the
662 SOCRATES airborne data (Figs. 1b-f, 2b-f).

663 Fig. 13 compares TOA RSW (a) and OLR (b) from CERES SYN observations
664 with the two models for the same period during CAPRICORN2. The deep clouds in
665 CAM6 tend to reflect more shortwave radiation (are 'brighter') than observed, leading to
666 a 10% high bias in the mean reflected SW over the whole period. The CAM6 OLR has a
667 time-mean comparable to the observations but has a low bias in the deep cloud regions
668 (e.g., Feb. 1-3, 11). In AM4 the RSW is comparable to CERES with intermittent high
669 biases, while the OLR is typically slightly high. Overall, these biases are similar to those
670 discussed in Section 3.3 for low clouds observed in SOCRATES. They imply that deep
671 clouds, like low clouds, are in general too bright in both CAM6 and AM4, and are too
672 frequent in CAM6 but too broken in AM4.

673

674 **4.2 Comparison of observed and simulated radar reflectivities**
675
676 Fig. 14 shows reflectivities from the CAM6 and AM4 COSP simulators for the
677 CAPRICORN2 campaign. For this study, CAM6 COSP provided reflectivity with and
678 without hydrometeor and gas attenuation as viewed from the ground (Figs. 14a and 14b),
679 while AM4 COSP only output attenuated reflectivity as viewed from space (Fig. 14c). As
680 seen by comparing Figs. 14a and 14b, the inclusion of attenuation can reduce the
681 reflectivity by several dB for deep precipitating clouds, but it has no significant impact on
682 cloud morphology and low cloud reflectivity. Since AM4 COSP reflectivity is
683 significantly weaker than that of CAM6 COSP (Fig. 14c), the hydrometeor attenuation is
684 of only minor importance. As such, we expect the space-based attenuated reflectivity of

AM4 COSP to be qualitatively comparable to its ground-based counterpart. In the rest of the study, unless otherwise mentioned, we will compare attenuated CAM6 and AM4 COSP reflectivity with observations.

CAM6 COSP reflectivity (Fig. 14b) agrees fairly well with the ship-observed reflectivity (Figs. 12a), but has longer and less interrupted periods of deep cloud occurrence (e.g., Feb. 1-3; Feb. 11-13). The AM4 COSP reflectivity is significantly too weak in the deep clouds, indicating underestimation of snow (Fig. 14c), for reasons to be discussed in Section 4.3. An abrupt change in reflectivity occurs at the freezing level at 1-2 km, below which the AM4 COSP reflectivity matches the observations better.

4.3 Low and deep clouds

For a quantitative statistical comparison of observed and modeled reflectivity, we construct Contoured Frequency by Altitude Diagrams (CFADs, Yuter and Houze, 1995) of observed and COSP reflectivity along the entire ship track during the CAPRICORN2 campaign (Fig. 15). The joint histograms are created for every 2 hours with a 100 m vertical resolution and 2 dBZ increments from -40 dBZ to 10 dBZ in the horizontal, then conditionally averaged over the desired cloud regimes. Unlike in some studies of deep convection (e.g., Houze et al., 2007), our CFADs are not normalized to exclude regions with no detectable reflectivity.

The CFAD averaged over all CAPRICORN2 observations (Fig. 15a) shows a shadowy boomerang shape with a horizontal arm due to low clouds below 4 km and a diagonal arm due to deep convective clouds that extend beyond 6 km. The CAM6 COSP

CFAD (Fig. 15b) displays a shape analogous to observations but with much higher occurrence of reflectivities exceeding -10 dBZ. The upper arm of the AM4 COSP reflectivity CFAD is strongly shifted by ~25 dBZ toward reflectivities lower than observed (Fig. 15c).

Fig. 15 also shows separate CFADs for low vs. deep cloud columns, which are defined as having a maximum reflectivity above 4 km less (vs. greater) than -40 dBZ. The observed low-cloud CFAD (Fig. 15d) has a mode between -10 and 0 dBZ between 0-1 km in altitude associated with lightly precipitating cloud, with a lower tail extending to -40 dBZ contributed by low-level non-precipitating clouds. The CAM6 low-cloud CFAD (Fig. 15e) shows a comparable histogram of reflectivities, but with the maximum occurrence frequency at a slightly lower reflectivity near -10 dBZ and no tail of reflectivities below -20 dBZ and 1 km altitude. The AM4 low-cloud CFAD (Fig. 15f) is fairly similar to observations below 1 km altitude but underestimates reflectivities above 1 km altitude.

The observed deep-cloud CFAD (Fig. 15g) constitutes the broader upper arm of the boomerang, with typical reflectivities clustering around 0 dBZ below 4 km and decreasing to ~ -20 dBZ at ~6 km (Fig. 15g). The CAM6 deep clouds (Fig. 15h) cluster at a comparable reflectivity range but occur more frequently than observed. Larger reflectivities are maintained at a much higher altitude in CAM6 as well. The AM4 deep clouds (Fig. 15i) have a -15 dBZ low bias in reflectivity except near the surface, where they are comparable in frequency and magnitude to observations.

4.4 Hydrometer microphysics inferred from COSP reflectivity decomposition

731 *4.4.1 CAM6*

732 To better understand the contributions of different hydrometeors in CAM6 to
733 reflectivity, we partition the non-attenuated COSP synthetic reflectivity into contributions
734 from cloud liquid, cloud ice, rain and snow. Here we only consider large-scale
735 precipitation, since convective precipitation rarely occurs in CAM6 along the ship track.
736 The synthetic reflectivities of liquid, ice and rain are calculated from their respective grid
737 mean number concentrations and effective radii following the formulas in COSP. The
738 synthetic snow reflectivity is computed as the residual of the total nonattenuated COSP
739 reflectivity and the sum of synthetic reflectivities from the other three hydrometers. AM4
740 only outputs an attenuated reflectivity which cannot be exactly partitioned in this way.

741 We decompose the CAPRICORN2 CAM6 CFADs into cloud liquid, cloud ice,
742 rain, and snow for all clouds (Fig. 16 a-d), low clouds (Fig. 16 e-h), and deep clouds (Fig.
743 16 i-l). In all cases, stronger reflectivities are dominated by snow. CAM6 also simulates
744 a substantial amount of cloud liquid with reflectivity below -20 dBZ and drizzle with
745 reflectivity below -20 dBZ at altitudes below 2 km (Fig. 16a, e, i). Above 2 km, cloud ice
746 becomes more prevalent in CAM6 but has low reflectivity below -10 dBZ. However,
747 such low reflectivity is missing in the non-partitioned reflectivity (Figs. 15b, e, and h)
748 suggesting that snow is more frequent in CAM6 than in the observations. The missing tail
749 of low reflectivities might be also partly due to the insufficient sub-grid variability of
750 cloud and precipitation in CAM6 COSP such that almost all simulated clouds have
751 precipitation dominating their reflectivity.

752 The snow mass or size in CAM6 low clouds appears underestimated since its
753 maximum frequency (Fig. 16h) is located at a lower reflectivity than the observations

754 (Fig. 15d). This indicates that snow in CAM6 low clouds is more homogeneous but less
755 intense compared to the observations. For deep clouds, the frequency of occurrence of
756 snow (Fig. 16l) is much higher than observations, while the grid average reflectivity is
757 similar to observed at ~ 0dBZ. This implies that the snow in CAM6 deep clouds is
758 similarly homogeneous and moderate. Note that the high snow occurrence could partially
759 be attributed to the insufficient sub-grid variability of cloud and precipitation in CAM6
760 COSP as mentioned earlier.
761
762 *4.4.2 AM4*
763 To better understand the representation of hydrometeors in AM4, we compare
764 time-height sections of grid mean liquid water and ice mixing ratios and precipitation
765 fluxes from CAM6 and AM4 (Fig. 17). Normally AM4 shows substentially more cloud
766 ice compared to CAM6 (Fig. 17f compared to b). The reason is that its microphysics
767 scheme does not distinguish snow from ice and the cloud ice in AM4 is the sum of ice
768 and snow. The AM4 downward ice flux is vertically continuous with the rain flux (Fig.
769 17 g to c), confirming that above the freezing level the AM4 precipitation from deep and
770 shallow clouds is in the form of sedimenting cloud ice particles. The snow flux
771 approximated from the clear-sky ice flux as used in AM4 COSP (Fig. 17h) is less
772 frequent and intense compared to the snow flux in CAM6 (Fig. 17d). AM4 has less
773 supercooled liquid water above 2 km than CAM6 (Fig. 17 e to a), but our CAPRICORN2
774 and SOCRATES observational analyses cannot as yet clearly test which model is closer
775 to the truth.

To evaluate the snow intensity in AM4, we compare the hydrometeor PSDs in AM4 COSP with CAM6 COSP (Fig. 18). Here the PSDs are computed from area-weighted mean cloud liquid, cloud ice, rain and snow. AM4 has greater ice with much less rain and snow. Compared with CAM6 COSP snow PSDs, AM4 COSP significantly underestimates large snow particles with radius greater than 100 microns, leading to lower reflectivities. The AM4 COSP snow PSD is not taken from the AM4 microphysics, which would give no separate snow contribution to the PSD and worsen the AM4 underestimate of reflectivity.

5. Summary

Observations of cloud properties from sophisticated in-situ and ship-based remote and in-situ sensors over the Southern Ocean during airborne (SOCRATES) and ship-based (CAPRICORN2) measurement campaigns during Jan.-Feb. 2018 are used to evaluate two state of the art atmospheric general circulation models (GCMs): CAM6 and AM4. These GCMs were nudged to reanalysis wind and temperature fields to minimize differences between modeled and observed synoptic conditions.

These measurements, together with collocated CERES TOA radiative flux estimates, provide a valuable dataset for evaluating simulations of cloud and precipitation in CAM6 and AM4 and to understand their radiation biases The major conclusions and implications are:

1. The nudged-meteorology simulation method facilitates detailed comparison of measured and simulated cloud properties from a limited set of observations in a synoptically variable environment.

2. Both GCMs correctly simulate that Southern Ocean supercooled boundary-layer clouds in that they reproduce observed compositions (i.e. they are mostly composed of small cloud droplets and larger precipitating ice particles).
3. CAM6 has too much cloud and that cloud is too bright ("too frequent, too bright").
4. Cloud droplet number concentration in CAM6 is typically too low.
5. Precipitation in CAM6 is too frequent and too homogeneous.
6. AM4 has too little cloud occurrence, but the clouds are too bright ("too few, too bright").
7. AM4 clouds include too much small ice and too little snow.

The low bias in cloud droplet number concentration in CAM6 is consistent with discrepancies seen between other state of the art models and satellite observations of Southern Ocean cloud droplet number concentrations in summertime low clouds (McCoy et al. 2020a in review, Revell et al. 2019). This low bias is a widespread issue remaining in GCMs that presumably contributes to TOA SW bias for low-lying liquid clouds over the Southern Ocean.

Both CAM6 COSP and AM4 COSP make assumptions about microphysics, size distributions, and horizontal homogeneity that are not fully consistent with their host GCM. Ideally such assumptions should be minimized, but at a minimum they must be kept in mind when comparing cloud radar data with COSP output. CAM6 COSP seems to simulate too large an area fraction of snow. AM4 simulates snow as a tail of the cloud ice distribution, while COSP expects a separate snow category. With or without COSP,

this results in AM4 simulating snow crystals that are too small and have far too little radar reflectivity.

The biggest challenge is still ahead – how to use the insights from this comprehensive analysis to improve the participating GCMs and their COSP simulators. We hope that the approach presented here will prove beneficial in testing other GCMs and developing improvements for future GCM versions.

Appendix A: HSRL backscatter coefficient threshold in determining cloud occurrence

HSRL obtains the lidar return signal with high spectral resolution (<75 MHz laser bandwidth), which enables the separation of aerosol and cloud returns from molecular returns. Here we further separate cloud from aerosol returns by use of calibrated HSRL aerosol and cloud backscatter coefficient.

Examining the probability density function of HSRL cloud and aerosol backscatter coefficient for all 15 flights during SOCRATES (Fig. A1), we find a tri-modal distribution with three peaks locating near 10^{-7}, 10^{-6}, and 10^{-3} $m^{-1}sr^{-1}$ respectively. Through inspection of HSRL lidar backscatter profiles (e.g., Figs. 4a and 4b), we interpret the two left modes as being contributed by the aerosols within and outside of the boundary layer, which are associated with lower backscatter coefficient than the rightmost cloud mode. We determine $3x10^{-5}$ $m^{-1}sr^{-1}$ as a HSRL

backscatter coefficient threshold separating the cloud mode from the two aerosol modes (the blue line in Fig. A1). This threshold was determined by a sensitivity test where we compare the HCR and HSRL cloud detection using different HSRL backscatter thresholds ranging from 10^{-5} to 10^{-4} $m^{-1}sr^{-1}$. We find that the frequency of cloud occurrence as detected by HSRL is not sensitive to the threshold, but reduces quickly once the threshold increases beyond $3x10^{-5}$ $m^{-1}sr^{-1}$.

Appendix B: Droplet size distribution in CAM6 microphysics scheme and CAM6 COSP

Use of CFADs as an observational constraint on GCM snowfall rate is complicated because the hydrometeor size distributions assumed in COSP do not match the internal distributions within the GCM microphysics. Here we compare CAM6 and CAM6 COSP DSDs for low clouds during CAPRICORN2 based on their respective hydrometeor size distribution assumptions described in Section 2.7 (Fig. 18). The hydrometeor PSDs are computed from their fraction mean masses and effective radii. Here we compare CAM6 microphysics and CAM6 COSP here, since AM4 COSP snow is not taken from the AM4 microphysics.

Rain and snow DSDs are represented well in CAM6 COSP. COSP slightly underestimates cloud liquid and overestimates ice particles, which leads to an underestimation (overestimation) in liquid (ice) reflectivities. However, this bias is not expected to significantly alter the net synthetic reflectivities in the frequently

precipitating CAM6 mixed–phased low clouds during CAPRICORN2 where snow dominates the reflectivity. A discrepancy is found for snow DSDs between CAM6 and CAM6 COSP, where CAM6 COSP has a greater concentration of small snowflakes (Fig. 18d). We note that this discrepancy is caused by the inconsistency in snow densities assumed in CAM6 and CAM6 COSP. CAM6 COSP assumes a snow density of 100 kg/m^3, but the effective radius used by CAM6 COSP is computed in CAM6 by assuming a snow density of 250 kg/m^3. The bigger snow density leads to a smaller effective radius, and therefore more small snowflakes and less big ones. Such discrepancy vanishes when the snow effective radius input into COSP is computed using a snow density of 100 kg/m^3 (not shown). The density inconsistency barely affects the large particle number and has little impact on reflectivity.

It is reasonable to assume that the snow size distributions during CAPRICORN2 are similar to that during SOCRATES. Comparing Figs. 8 and 18 suggests that the mean snow PSD in CAM6 including all cloud types in SOCRATES is on average qualitatively consistent with the mean SOCRATES-observed DSD for precipitating low clouds, although the frequency of occurrence of snow is much higher.

Acknowledgement:

This work is funded by U.S. National Science Foundation (NSF) award numbers AGS-1660604 and AGS-1660609. The authors thank the National Center for Atmospheric Research (NCAR, supported by NSF) Earth Observing Laboratory (EOL) and CSIRO Marine National Facility (MNF) for supporting and undertaking the SOCRATES and

CAPRICORN2 deployment. We acknowledge the teams of SOCRATES and CAPRICORN2 scientists and technicians who made this work possible by collecting the data and maintaining the instruments. SOCRATES data are provided by EOL at https://data.eol.ucar.edu/. We thank Alain Protat (alain.protat@bom.gov.au) for providing radar reflectivity data during CAPRICORN2. CIRES SYN data used in this study were obtained from the NASA Earth Science Data Systems program: https://search.earthdata.nasa.gov.

References

Abdelmotaleb, A., Järvinen, E., Duft, D., Hirst, E., Vogt, S., Leisner, T., & Schnaiter, M. (2016). PHIPS-HALO: the airborne Particle Habit Imaging and Polar Scattering probe-Part 1: Design and operation. *Atmospheric Measurement Techniques*.

Atlas R. L., Bretherton C. S., and P. N. Blossey (2020) How well do high and low resolution models represent observed boundary layer structures and low clouds over the summertime Southern Ocean? *Journal of Geophysical Research: Atmospheres (submitted).*

Bodas-Salcedo, A., Webb, M. J., Bony, S., Chepfer, H., Dufresne, J. L., Klein, S. A., ... & John, V. O. (2011). COSP: Satellite simulation software for model assessment. *Bulletin of the American Meteorological Society*, ***92***(8), 1023-1043.

Bodas-Salcedo, A., Williams, K. D., Ringer, M. A., Beau, I., Cole, J. N., Dufresne, J. L., ... & Yokohata, T. (2014). Origins of the solar radiation biases over the Southern Ocean in CFMIP2 models. *Journal of Climate*, *27*(1), 41-56.

Bodas-Salcedo, A., Mulcahy, J. P., Andrews, T., Williams, K. D., Ringer, M. A., Field, P. R., & Elsaesser, G. S. (2019). Strong dependence of atmospheric feedbacks on mixed-phase microphysics and aerosol-cloud interactions in HadGEM3. *Journal of Advances in Modeling Earth Systems*.

Bogenschutz, P. A., Gettelman, A., Morrison, H., Larson, V. E., Craig, C., & Schanen, D. P. (2013). Higher-order turbulence closure and its impact on climate simulations in the Community Atmosphere Model. *Journal of Climate*, ***26***(23), 9655-9676.

Bogenschutz, P. A., Gettelman, A., Hannay, C., Larson, V. E., Neale, R. B., Craig, C., & Chen, C. C. (2018). The path to CAM6: Coupled simulations with CAM5. 4 and CAM5. 5. *Geoscientific Model Development (Online)*, *11*(LLNL-JRNL-731418).

Bony, S., & Dufresne, J. L. (2005). Marine boundary layer clouds at the heart of tropical cloud feedback uncertainties in climate models. *Geophysical Research Letters*, *32*(20).

Bretherton, C. S., McCoy, I. L., Mohrmann, J., Wood, R., Ghate, V., Gettelman, A., ... & Zuidema, P. (2019). Cloud, aerosol, and boundary layer structure across the northeast Pacific stratocumulus–cumulus transition as observed during CSET. *Monthly Weather Review*, *147*(6), 2083-2103.

Ceppi, P., Hwang, Y. T., Frierson, D. M., & Hartmann, D. L. (2012). Southern Hemisphere jet latitude biases in CMIP5 models linked to shortwave cloud forcing. *Geophysical Research Letters*, *39*(19).

Cess, R. D., Zhang, M. H., Ingram, W. J., Potter, G. L., Alekseev, V., Barker, H. W., ... & Dix, M. R. (1996). Cloud feedback in atmospheric general circulation models: An update. *Journal of Geophysical Research: Atmospheres*, *101*(D8), 12791-12794.

Doelling, D. R., Loeb, N. G., Keyes, D. F., Nordeen, M. L., Morstad, D., Nguyen, C., ... & Sun, M. (2013). Geostationary enhanced temporal interpolation for CERES flux products. *Journal of Atmospheric and Oceanic Technology*, *30*(6), 1072-1090.

Donner, L. J., Seman, C. J., Soden, B. J., Hemler, R. S., Warren, J. C., Ström, J., & Liou, K. N. (1997). Large-scale ice clouds in the GFDL SKYHI general circulation model. *Journal of Geophysical Research: Atmospheres*, *102*(D18), 21745-21768.

Dunne et al. (2019). Model description and simulation characteristics. Journal of Advances in Modeling Earth Systems. (submitted)

UCAR/NCAR - Earth Observing Laboratory. (2005). NSF/NCAR GV HIAPER Aircraft. UCAR/NCAR - Earth Observing Laboratory. https://doi.org/10.5065/D6DR2SJP Retrieved December 14, 2016

SouthWest Sciences, I. (SWS), & UCAR/NCAR - Earth Observing Laboratory. (2008). Vertical Cavity Surface-Emitting Laser (VCSEL) Hygrometer. UCAR/NCAR - Earth Observing Laboratory. https://doi.org/10.5065/D6PV6HDM Retrieved December 20, 2016

UCAR/NCAR - Earth Observing Laboratory, & University of Wisconsin. (2010). High Spectral Resolution Lidar for the Gulfstream-V; G5-HSRL. UCAR/NCAR - Earth Observing Laboratory. https://doi.org/10.5065/D67W6976 Retrieved December 20, 2016

UCAR/NCAR - Earth Observing Laboratory. (2014). HIAPER Cloud Radar (HCR). UCAR/NCAR - Earth Observing Laboratory. https://doi.org/10.5065/D6BP00TP Retrieved December 20, 2016

Engström, A., Bender, F. M., Charlson, R. J., & Wood, R. (2015). The nonlinear relationship between albedo and cloud fraction on near-global, monthly mean scale in observations and in the CMIP5 model ensemble. *Geophysical Research Letters*, *42*(21), 9571-9578.

Eyring, V., Bony, S., Meehl, G. A., Senior, C., Stevens, B., Stouffer, R. J., & Taylor, K. E. (2015). Overview of the Coupled Model Intercomparison Project Phase 6 (CMIP6) experimental design and organisation. *Geoscientific Model Development Discussions*, *8*(12).

Gettelman, A., & Morrison, H. (2015). Advanced two-moment bulk microphysics for global models. Part I: Off-line tests and comparison with other schemes. *Journal of Climate*, ***28***(3), 1268-1287.

Gettelman, A., Hannay, C., Bacmeister, J. T., Neale, R. B., Pendergrass, A. G., Danabasoglu, G., ... & Mills, M. J. (2019). High climate sensitivity in the Community Earth System Model Version 2 (CESM2). *Geophysical Research Letters*.

Gettelman, A., Bardeen C. G., McCluskey C. S., Jävinen E., Stith J., Bretherton C. (2020). Simulating Observations of Southern Ocean Clouds and Implications for Climate. *Journal of Geophysical Research: Atmospheres. (submitted)*

Gordon, N. D., & Klein, S. A. (2014). Low-cloud optical depth feedback in climate models. *Journal of Geophysical Research: Atmospheres*, *119*(10), 6052-6065.

Guo, H., Golaz, J. C., Donner, L. J., Ginoux, P., & Hemler, R. S. (2014). Multivariate probability density functions with dynamics in the GFDL atmospheric general circulation model: Global tests. *Journal of Climate*, *27*(5), 2087-2108.

Guo, H., Golaz, J. C., Donner, L. J., Wyman, B., Zhao, M., & Ginoux, P. (2015). CLUBB as a unified cloud parameterization: Opportunities and challenges. *Geophysical Research Letters*, ***42***(11), 4540-4547.

Haynes, J. M., Marchand, R. T., Luo, Z., Bodas-Salcedo, A., & Stephens, G. L. (2007). A multipurpose radar simulation package: QuickBeam. *Bulletin of the American Meteorological Society*, *88*(11), 1723-1728.

Held, I. M., et al. (2019). Structure and performance of GFDL's CM4.0 climate model. *J. Adv. Model. Earth Syst.*, **11**, 3691– 3727. https://doi.org/10.1029/2019MS001829

Hersbach, H., and D. Dee, 2016: ERA-5 reanalysis is in pro-duction.ECMWF Newsletter, No. 147, ECMWF, Reading, United Kingdom,https://www.ecmwf.int/en/newsletter/147/news/era5-reanalysis-production

Hoose, C., Kristjansson, J. E., Chen, J.-P., & Hazra, A. (2010, March). A Classical-Theory-Based Parameterization of Heterogeneous Ice Nucleation by Mineral Dust, Soot, and Biological Particles in a Global Climate Model. J. Atmos. Sci., 67 (8), 2483-2503. doi: 10.1175/2010JAS3425.1

Houze Jr, R. A., Wilton, D. C., & Smull, B. F. (2007). Monsoon convection in the Himalayan region as seen by the TRMM Precipitation Radar. *Quarterly Journal of the Royal Meteorological Society: A journal of the atmospheric sciences, applied meteorology and physical oceanography*, *133*(627), 1389-1411.

Hwang, Y. T., Frierson, D. M., & Kang, S. M. (2013). Anthropogenic sulfate aerosol and the southward shift of tropical precipitation in the late 20th century. *Geophysical Research Letters*, *40*(11), 2845-2850.

Jeuken, A. B. M., Siegmund, P. C., Heijboer, L. C., Feichter, J., & Bengtsson, L. (1996). On the potential of assimilating meteorological analyses in a global climate model for the purpose of model validation. *Journal of Geophysical Research: Atmospheres*, ***101***(D12), 16939-16950.

Kay, J. E., Wall, C., Yettella, V., Medeiros, B., Hannay, C., Caldwell, P., & Bitz, C. (2016). Global climate impacts of fixing the Southern Ocean shortwave radiation bias in the Community Earth System Model (CESM). *Journal of Climate*, *29*(12), 4617-4636.

Kollias, P., Clothiaux, E. E., Miller, M. A., Albrecht, B. A., Stephens, G. L., & Ackerman, T. P. (2007). Millimeter-wavelength radars: New frontier in atmospheric cloud and precipitation research. *Bulletin of the American Meteorological Society*, *88*(10), 1608-1624.

Liu, X., Ma, P. L., Wang, H., Tilmes, S., Singh, B., Easter, R. C., ... & Rasch, P. J. (2016). Description and evaluation of a new four-mode version of the Modal Aerosol Module (MAM4) within version 5.3 of the Community Atmosphere Model. *Geoscientific Model Development (Online)*, ***9***(PNNL-SA-110649).

Mace, G. G., & Zhang, Q. (2014). The CloudSat radar-lidar geometrical profile product (RL-GeoProf): Updates, improvements, and selected results. *Journal of Geophysical Research: Atmospheres*, *119*(15), 9441-9462.

Mace, G. G., & Protat, A. (2018). Clouds over the Southern Ocean as observed from the R/V Investigator during CAPRICORN. Part I: Cloud occurrence and phase partitioning. *Journal of Applied Meteorology and Climatology*, *57*(8), 1783-1803.

Mason, S., Jakob, C., Protat, A., & Delanoë, J. (2014). Characterizing observed midtopped cloud regimes associated with Southern Ocean shortwave radiation biases. *Journal of Climate*, *27*(16), 6189-6203.

Matrosov, S. Y. (2007). Potential for attenuation-based estimations of rainfall rate from CloudSat. *Geophysical research letters*, *34*(5).

McCoy, D. T., Tan, I., Hartmann, D. L., Zelinka, M. D., & Storelvmo, T. (2016). On the relationships among cloud cover, mixed-phase partitioning, and planetary albedo in GCMs. *Journal of Advances in Modeling Earth Systems*, *8*(2), 650-668.

McCoy, I. L., McCoy D. T., Wood R. Regayre L., Watson-Parris D., Grosvenor D. P., Mulcahy J. P., Hu Y., Bender F. A. –M., Field P. R., Carslaw K., Gordon H. (2020a). The hemispheric contrast in cloud microphysical properties constrains aerosol forcing. Proceedings of the National Academy of Sciences of the United States of America. Submitted.

McCoy I. L., Bretherton C. S., Wood R., Twohy C. H., Gettelman A., Bardeen C. (2020b). Recent Particle Formation and Aerosol Variability Near Southern Ocean Low Clouds. In preparation.

Meehl, G. A., Covey, C., McAvaney, B., Latif, M., & Stouffer, R. J. (2005). Overview of the coupled model intercomparison project. *Bulletin of the American Meteorological Society*, *86*(1), 89-93.

Ming, Y., Ramaswamy, V., Donner, L. J., & Phillips, V. T. J. (2005). A robust parameterization of cloud droplet activation. *J. Atmos. Sci*.

Ming, Y., Ramaswamy, V., Donner, L. J., Phillips, V. T., Klein, S. A., Ginoux, P. A., & Horowitz, L. W. (2007). Modeling the interactions between aerosols and liquid water clouds with a self-consistent cloud scheme in a general circulation model. *Journal of the Atmospheric Sciences*, *64*(4), 1189-1209.

Molod, A., Takacs, L., Suarez, M., & Bacmeister, J. (2015). Development of the GEOS-5 atmospheric general circulation model: Evolution from MERRA to MERRA2. *Geoscientific Model Development*, ***8***(5), 1339-1356.

Nam, C., Bony, S., Dufresne, J. L., & Chepfer, H. (2012). The 'too few, too bright'tropical low-cloud problem in CMIP5 models. *Geophysical Research Letters*, *39*(21).

Platnick, S., King, M. D., Ackerman, S. A., Menzel, W. P., Baum, B. A., Riédi, J. C., & Frey, R. A. (2003). The MODIS cloud products: Algorithms and examples from Terra. *IEEE Transactions on Geoscience and Remote Sensing*, *41*(2), 459-473.

Protat, A., Schulz, E., Rikus, L., Sun, Z., Xiao, Y., & Keywood, M. (2017). Shipborne observations of the radiative effect of Southern Ocean clouds. *Journal of Geophysical Research: Atmospheres*, *122*(1), 318-328.

Rienecker, M. M., Suarez, M. J., Gelaro, R., Todling, R., Bacmeister, J., Liu, E., ... & Bloom, S. (2011). MERRA: NASA's modern-era retrospective analysis for research and applications. *Journal of climate*, ***24***(14), 3624-3648.

Rotstayn, L. D. (1997). A physically based scheme for the treatment of stratiform clouds and precipitation in large-scale models. I: Description and evaluation of the microphysical processes. *Quarterly Journal of the Royal Meteorological Society*, *123*(541), 1227-1282.

Rotstayn, L. D. (2000). On the "tuning" of autoconversion parameterizations in climate models. *Journal of Geophysical Research: Atmospheres*, *105*(D12), 15495-15507.

Rutan, D. A., Kato, S., Doelling, D. R., Rose, F. G., Nguyen, L. T., Caldwell, T. E., & Loeb, N. G. (2015). CERES synoptic product: Methodology and validation of surface radiant flux. *Journal of Atmospheric and Oceanic Technology*, *32*(6), 1121-1143.

Schnaiter, M. 2018. PHIPS-HALO Stereo Imaging Data. Version 1.0. UCAR/NCAR - Earth Observing Laboratory. https://doi.org/10.5065/D62B8WWF. Accessed 14 Jan 2020.

Schnaiter, M., Järvinen, E., Ahmed, A., & Leisner, T. (2018). PHIPS-HALO: the airborne particle habit imaging and polar scattering probe–Part 2: Characterization and first results. *Atmospheric Measurement Techniques*, *11*(1), 341.

Shi, X., Liu, X., & Zhang, K. (2015, February). Effects of pre-existing ice crystals on cirrus clouds and comparison between different ice nucleation parameterizations with the Community Atmosphere Model (CAM5). Atmospheric Chemistry and Physics, 15 (3), 1503-1520. doi: 10.5194/acp-15-1503-2015

Swales, D. J., Pincus, R., & Bodas-Salcedo, A. (2018). The cloud feedback model intercomparison project observational simulator package: Version 2. *Geoscientific Model Development*, *11*(1), 77-81.

Song, H., Zhang, Z., Ma, P. L., Ghan, S., & Wang, M. (2018). The importance of considering sub-grid cloud variability when using satellite observations to evaluate the cloud and precipitation simulations in climate models. *UMBC Physics Department*.

Tan, I., Storelvmo, T., & Zelinka, M. D. (2016). Observational constraints on mixed-phase clouds imply higher climate sensitivity. *Science*, *352*(6282), 224-227.

Terai, C. R., Klein, S. A., & Zelinka, M. D. (2016). Constraining the low-cloud optical depth feedback at middle and high latitudes using satellite observations. *Journal of Geophysical Research: Atmospheres*, *121*(16), 9696-9716.

Tiedtke, M. (1993). Representation of clouds in large-scale models. *Monthly Weather Review*, *121*(11), 3040-3061.

Trenberth, K. E., & Fasullo, J. T. (2010). Simulation of present-day and twenty-first-century energy budgets of the southern oceans. *Journal of Climate*, *23*(2), 440-454.

UCAR/NCAR - Earth Observing Laboratory. (2005). NSF/NCAR GV HIAPER Aircraft. UCAR/NCAR - Earth Observing Laboratory. https://doi.org/10.5065/D6DR2SJP Retrieved December 14, 2016.

Wang, Y., Liu, X., Hoose, C., & Wang, B. (2014, October). Different contact angle distributions for heterogeneous ice nucleation in the Community Atmospheric Model version 5. *Atmos. Chem. Phys.*, 14 (19), 10411-10430. doi:10.5194/acp-14-10411-2014

Williams, K. D., Bodas-Salcedo, A., Déqué, M., Fermepin, S., Medeiros, B., Watanabe, M., ... & Williamson, D. L. (2013). The Transpose-AMIP II experiment and its application to the understanding of Southern Ocean cloud biases in climate models. *Journal of Climate*, *26*(10), 3258-3274.

Wexler, A. (1976). Vapor pressure formulation for water in range 0 to 100 C. A revision. *J. Res. Natl. Bur. Stand. A*, *80*, 775-785.

Wu, W., McFarquhar, G. 2019. NSF/NCAR GV HIAPER 2D-S Particle Size Distribution (PSD) Product Data. Version 1.1. UCAR/NCAR - Earth Observing Laboratory. https://doi.org/10.26023/8HMG-WQP3-XA0X. Accessed 14 Jan 2020.

Wielicki, B. A., Barkstrom, B. R., Harrison, E. F., Lee III, R. B., Smith, G. L., & Cooper, J. E. (1996). Clouds and the Earth's Radiant Energy System (CERES): An earth observing system experiment. *Bulletin of the American Meteorological Society*, *77*(5), 853-868.

Wu, C., Liu, X., Diao, M., Zhang, K., Gettelman, A., Lu, Z., Penner, J. E., and Lin, Z., 2017: Direct comparisons of ice cloud macro- and microphysical properties simulated by the Community Atmosphere Model version 5 with HIPPO aircraft observations, *Atmos. Chem. Phys*., **17**, 4731-4749, https://doi.org/10.5194/acp-17-4731-2017.

Yuter, S. E., & Houze Jr, R. A. (1995). Three-dimensional kinematic and microphysical evolution of Florida cumulonimbus. Part II: Frequency distributions of vertical velocity, reflectivity, and differential reflectivity. *Monthly weather review*, *123*(7), 1941-1963.

Zelinka, M. D., Myers, T. A., McCoy, D. T., Po-Chedley, S., Caldwell, P. M., Ceppi, P., ... & Taylor, K. E. (2020). Causes of higher climate sensitivity in CMIP6 models. *Geophysical Research Letters*, *47*(1), e2019GL085782.

Zhao, M., Golaz, J. C., Held, I. M., Ramaswamy, V., Lin, S. J., Ming, Y., ... & Guo, H. (2016). Uncertainty in model climate sensitivity traced to representations of cumulus precipitation microphysics. *Journal of Climate*, *29*(2), 543-560.

Zhao, M., Golaz, J. C., Held, I. M., Guo, H., Balaji, V., Benson, R., ... & Dunne, K. (2018). The GFDL global atmosphere and land model AM4.0/LM4.0: 2. Model description, sensitivity studies, and tuning strategies. *Journal of Advances in Modeling Earth Systems*, *10*(3), 735-769.

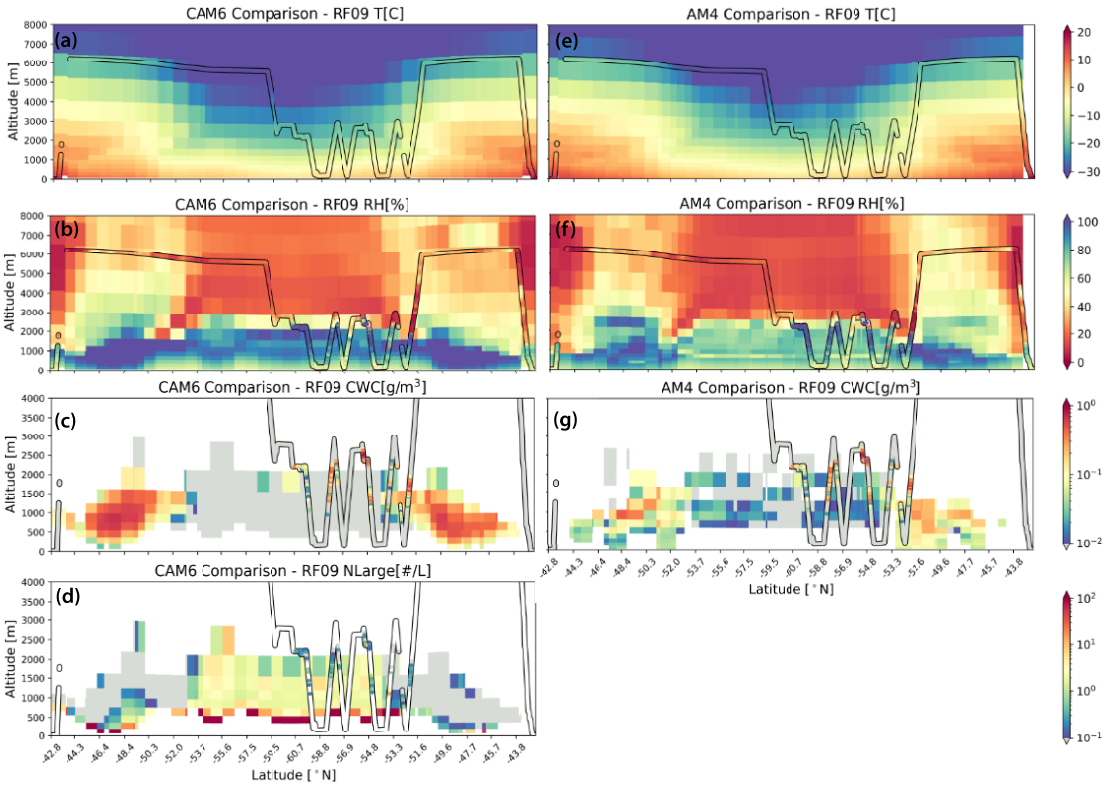
CAM6 Comparison - RF09 T[C]
AM4 Comparison - RF09 T[C]
CAM6 Comparison - RF09 RH[%]
AM4 Comparison - RF09 RH[%]
CAM6 Comparison - RF09 CWC[g/m^3]
AM4 Comparison - RF09 CWC[g/m^3]
CAM6 Comparison - RF09 NLarge[#/L]
(a)
(b)
(c)
(d)
(e)
(f)
(g)
Altitude [m]
Latitude [°N]

Fig. 1. SOCRATES flight RF09 observed (a) ambient temperature, (b) relative humidity, (c) liquid cloud water content from CDP, and (d) large particle number density NLarge (a precipitation indicator described in the text), shown as shading within black channels, overlying the corresponding CAM6 model output. (e)-(g): same as (a)-(c) but overlying profiles in AM4. NLarge cannot be computed from AM4 outputs. Gray shading denotes data that falls below the trusted value range. Missing data is shown either as gaps in the observation channel or in white.

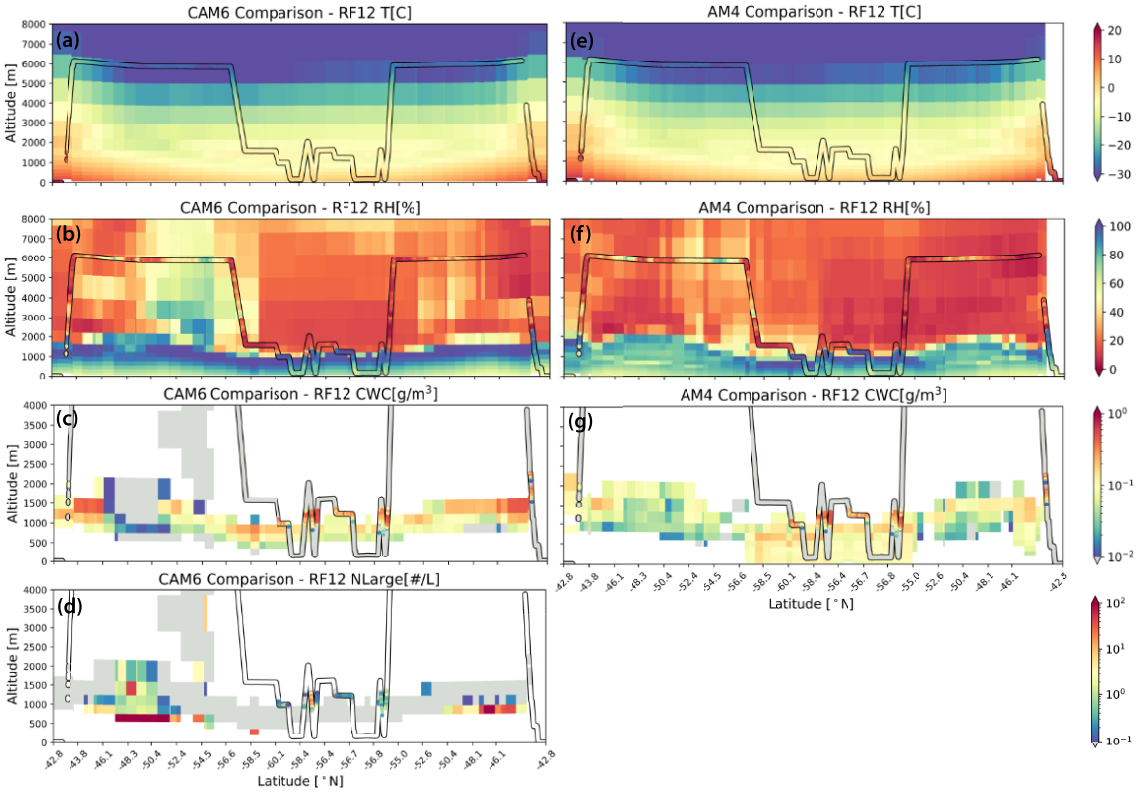

Fig. 2. Same as Fig. 1 but for flight RF12.

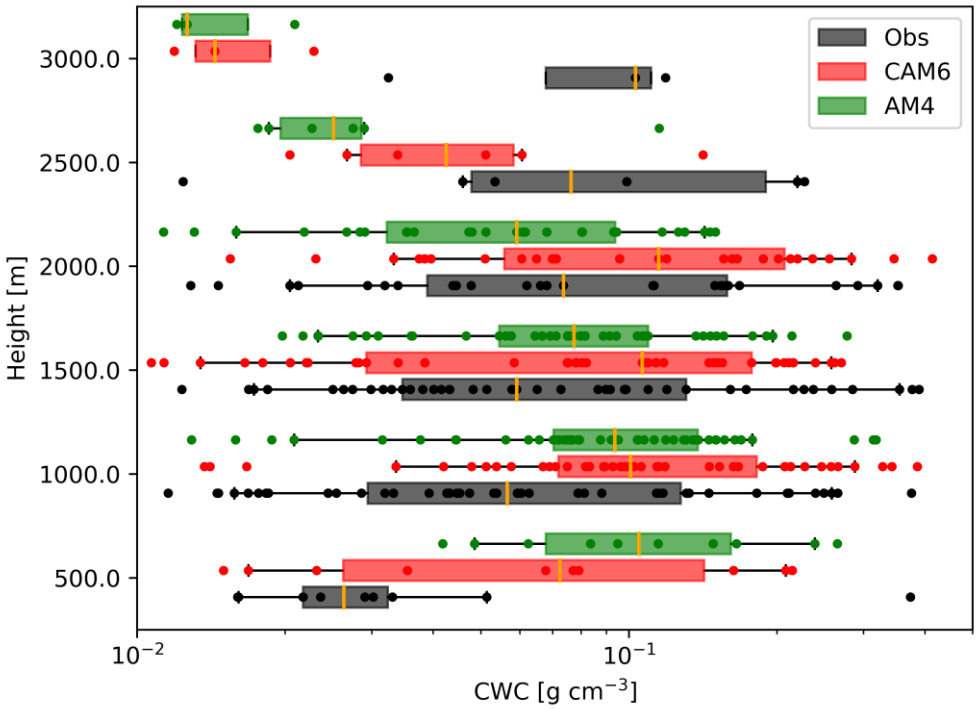

Fig. 3. Inter-quartile range boxes of observed and GCM in-cloud water content at different heights below 3 km for 15 flights during the SOCRATES campaign. Data is binned into boxes of 500 m in altitude and 25 minutes in time (dots) before range boxes are calculated. The orange bar inside the box indicates a median value for each bin and the whiskers indicate a range of 5-95%.

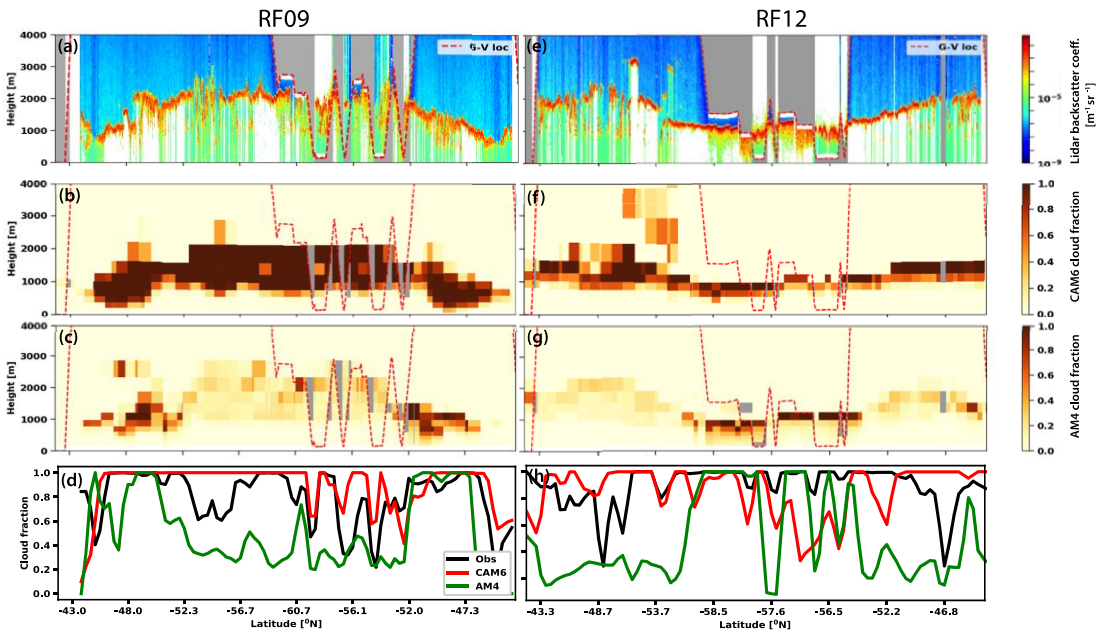

1220

1221 Fig. 4. (a) HSRL lidar backscatter coefficient, (b) CAM6 cloud fraction, (c) AM4 cloud

1222 fraction, and (d)) cloud occurrence below 4 km from observations, in CAM6, and AM4

1223 for SOCRATES flight RF09. Red dashed lines indicate the position of the GV aircraft.

1224 Gray shading indicates the area of no observations. HSRL backscatter within the dead

1225 zone extending 150 m from the aircraft is masked white. (e)-(h), same as (a)-(d) but for

1226 RF12.

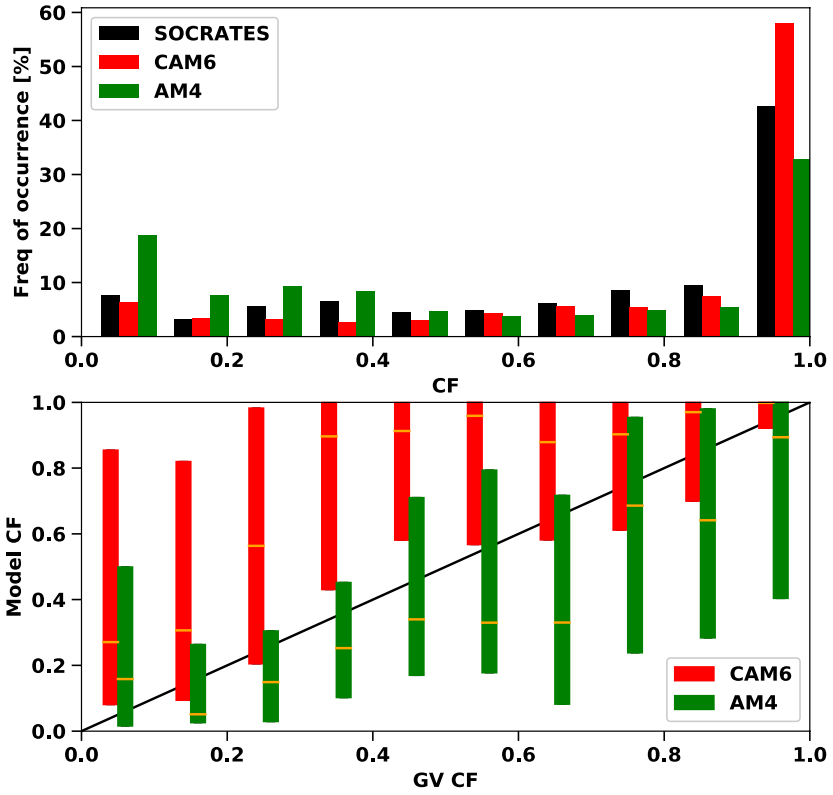

Fig. 5. (a) Frequency of occurrence of low clouds (below 4 km) from observations (black), CAM6 (red), and AM4 (green), and (b) inter-quartile range boxes of CAM6 and AM4 low cloud occurrence binned to 0.1 of observed low cloud fraction during SOCRATES. The orange bar inside each box indicates the bin-median.

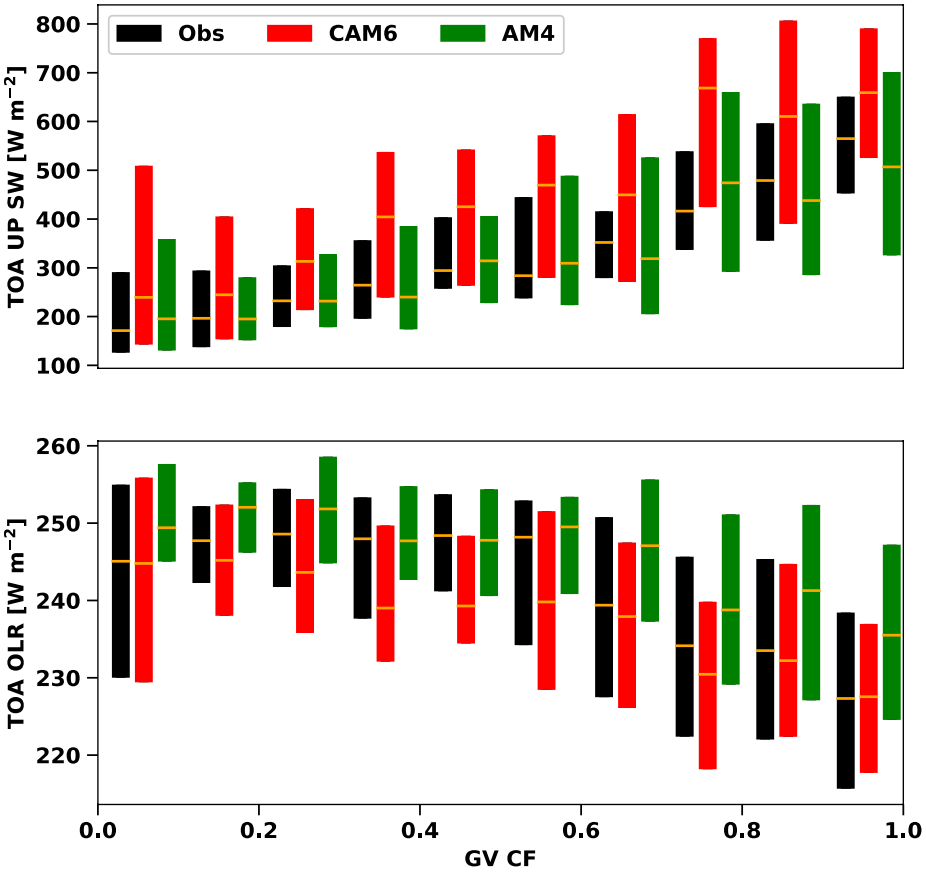

Fig. 6. Inter-quartile range boxes of observation matched CERES SYN (black), CAM6 (red), and AM4 (green) TOA (a) RSW scaled to insolation at solar noon and (b) OLR, averaged over bins of observed low cloud occurrence during SOCRATES. The orange bar inside the box indicates a bin-median.

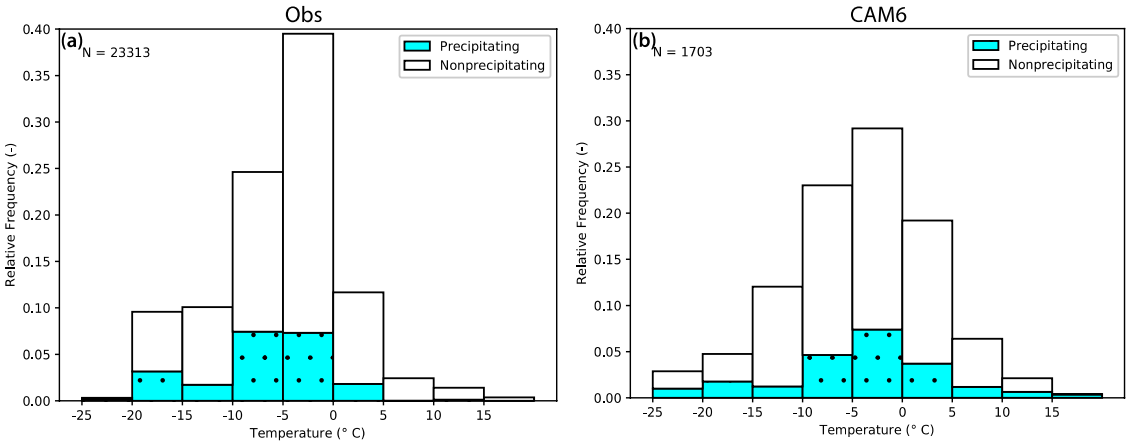

Fig. 7. Stacked histogram of occurrence frequency of (a) observed, and (b) CAM6 nonprecipitating and precipitating low clouds along the SOCRATES flight tracks, sorted by ambient temperature.

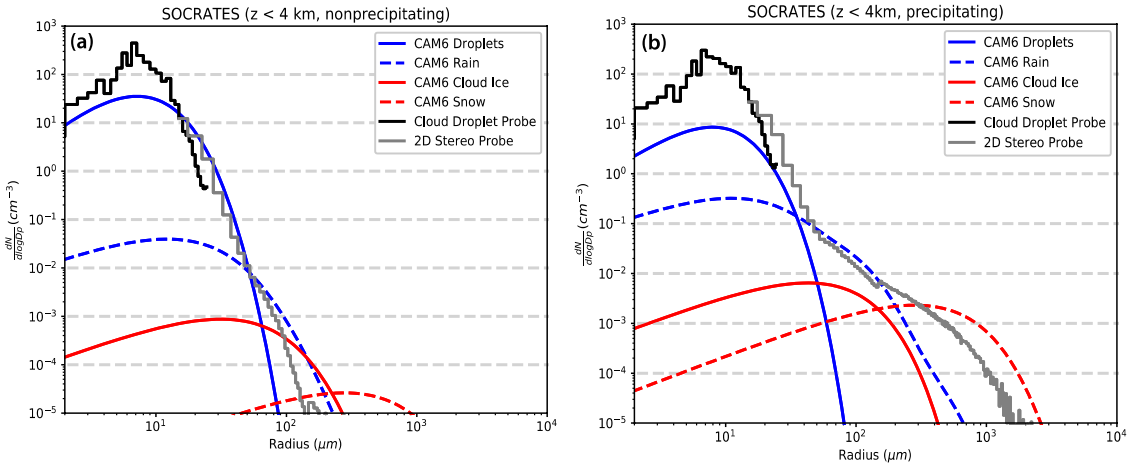

Fig. 8. Particle size distributions averaged across SOCRATES for CDP and 2DS observations (black lines) and CAM6 (colored lines) in (a) nonprecipitating low clouds, and (b) precipitating low clouds.

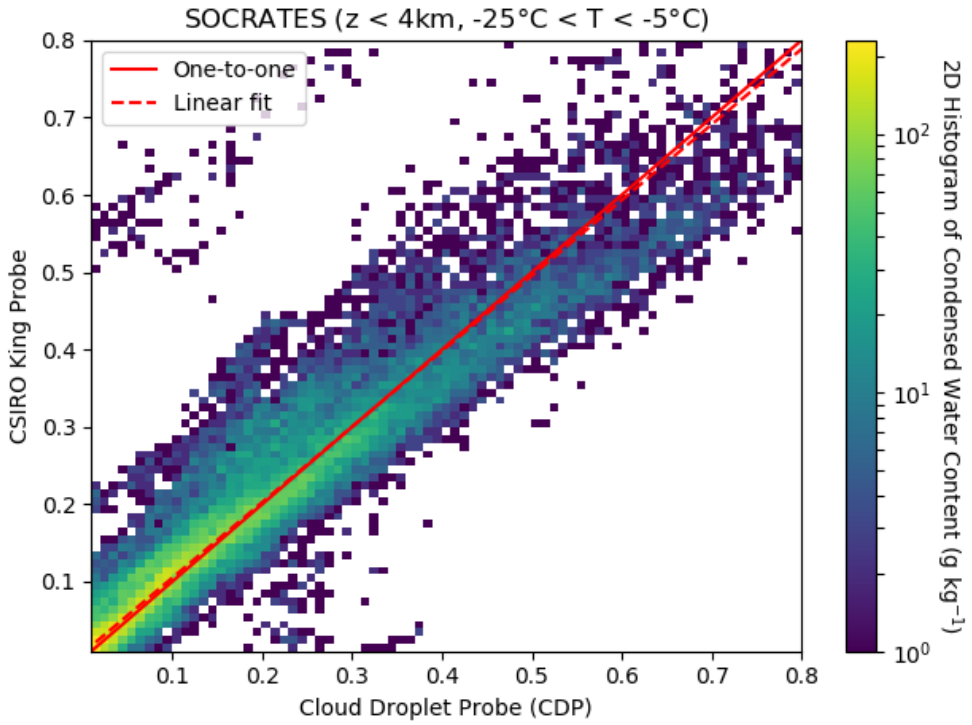

1246

1247 Fig. 9 2D histogram of condensed water content for cloud droplet probe and CSIRO

1248 King Probe for low clouds at temperature between -5 ºC and -25ºC.

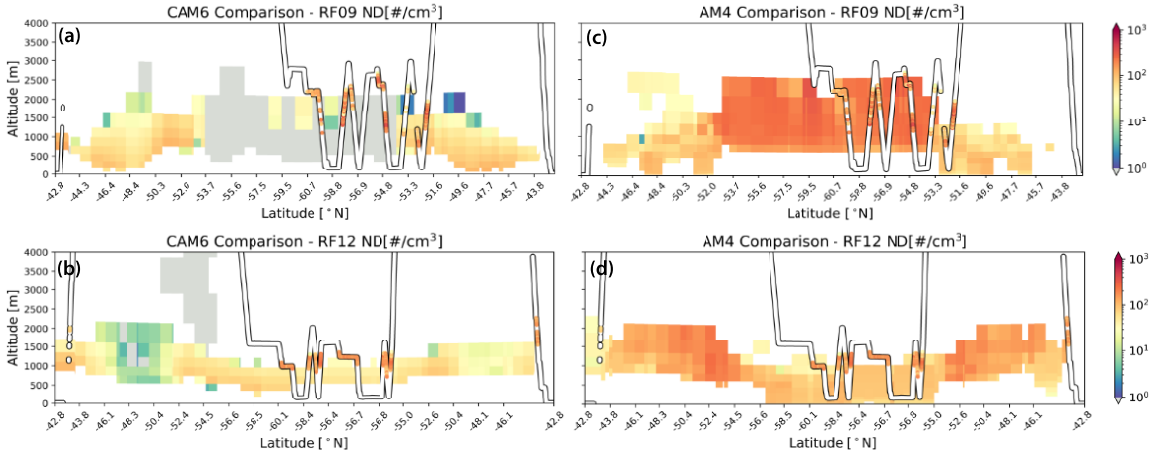

1249

Fig. 10 In-cloud CDP-derived droplet number concentration for SOCRATES flight RF09 and RF12 (shades inside black channels) overlying the corresponding variable profiles in CAM6 and AM4 as in Fig . 1 and 2.

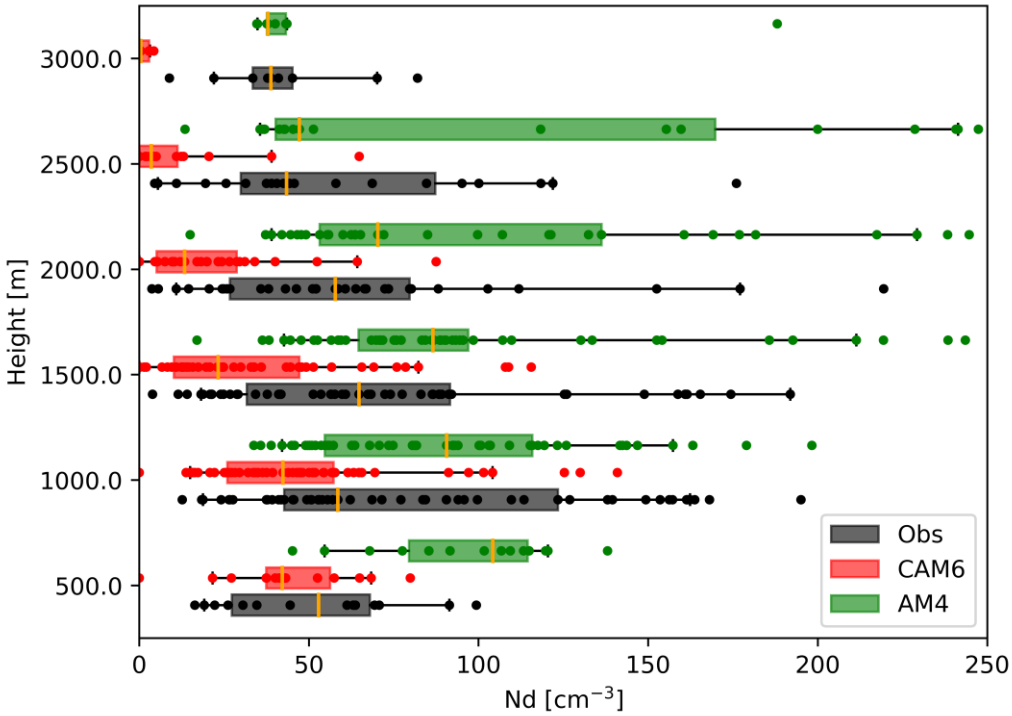

Fig. 11 Inter-quartile range boxes of observed and modeled in-cloud droplet number concentration binned into boxes of 500 m in altitude and 25 minutes in time (dots) before range boxes are calculated (as in Fig. 3). All in-cloud data (CWC>0.01 g m^{-3}) up to 3 km across all 15 SOCRATES flights is included in the bin mean calculation. Only average $N_d \geq 1$ cm^{-3} is used in calculating the range boxes. The orange bar inside the box indicates a bin-median and the whiskers indicate the 5-95% range.

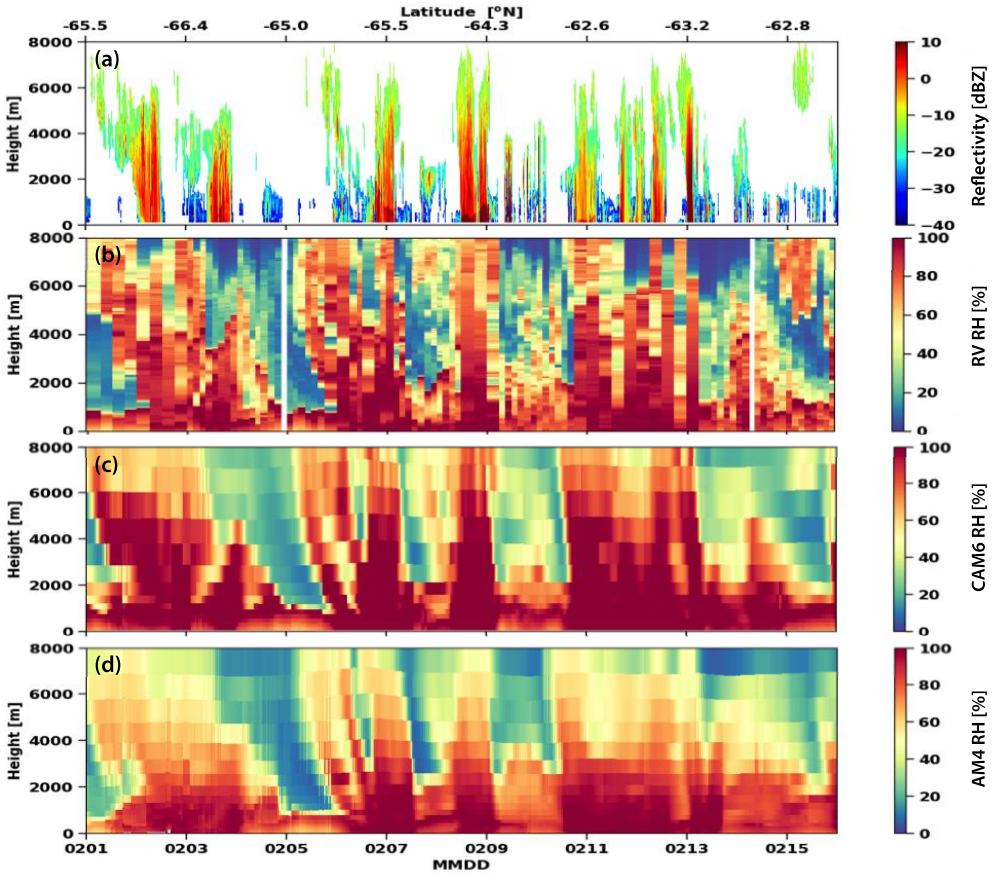

1260

1261 Fig. 12 (a) Ship-based upward-pointing W-band radar reflectivity, and relative humidity

1262 profiles from (b) radiosondes, (c) CAM6, and (d) AM4 during the 1-15 February 2018

1263 period of CAPRICORN2.

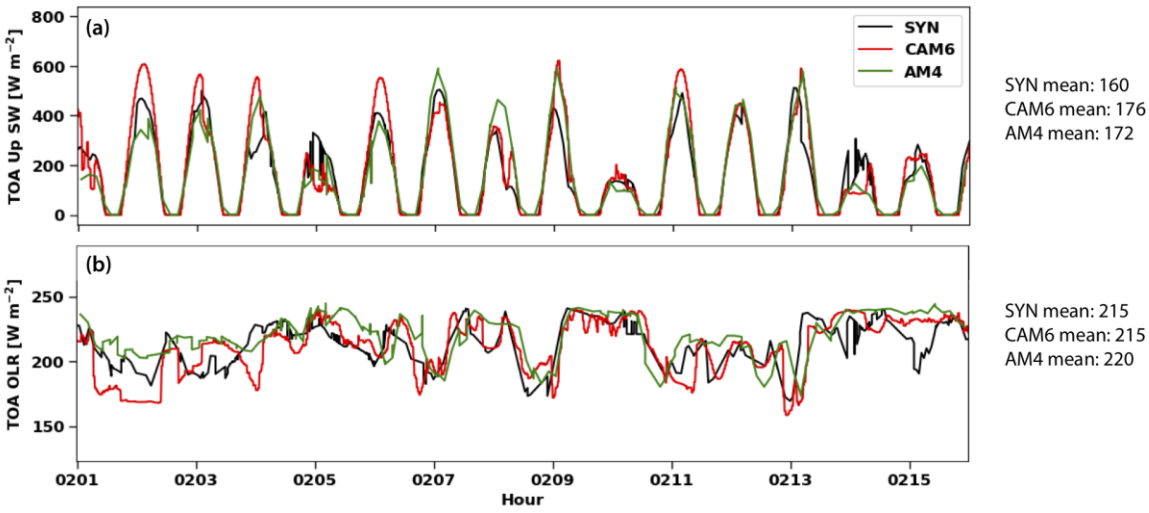

1264

Fig. 13 TOA (a) RSW and (b) OLR from CERES SYN observations (black), CAM6 (red), and AM4 (green) during the 1-15 February 2018 period of the CAPRICORN2 campaign.

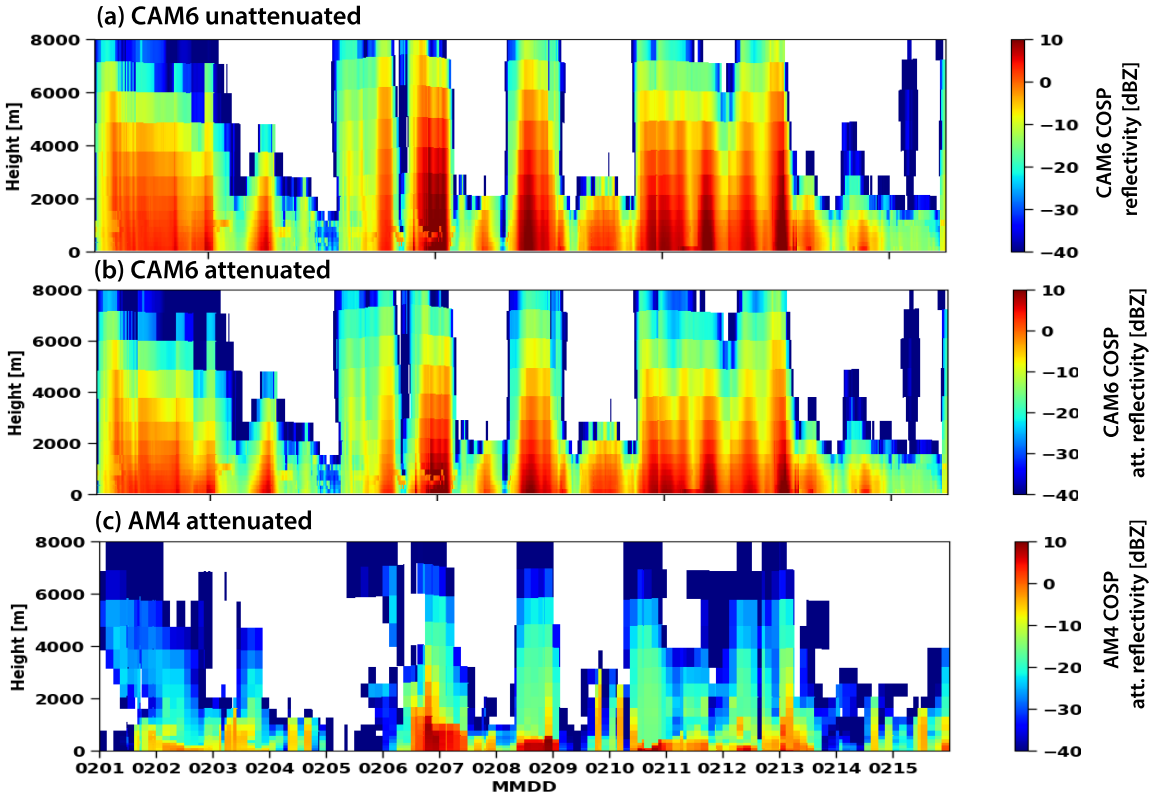

Fig. 14 (a) CAM6 COSP unattenuated reflectivity, (b) CAM6 COSP attenuated reflectivity as viewed from the ground, and (c) AM4 attenuated reflectivity as viewed from space, during the 1-15 February 2018 period of CAPRICORN2.

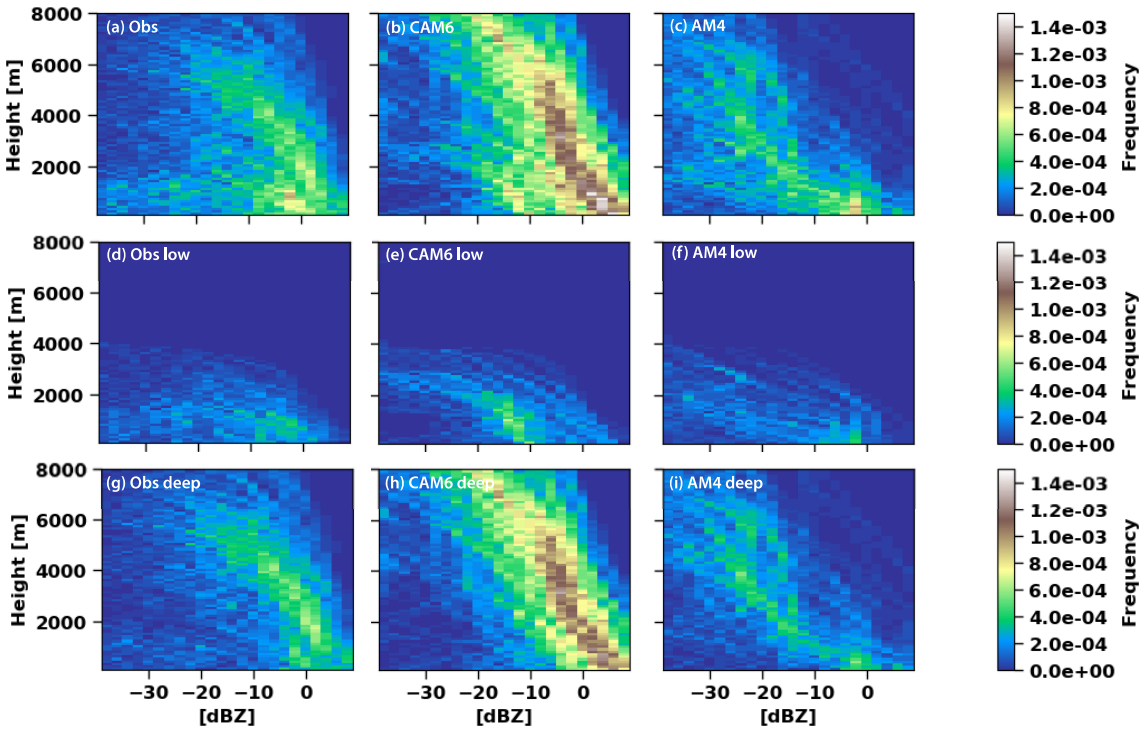

Fig. 15 Contoured frequency by altitude diagrams (CFADs; see text for details) encompassing the entire CAPRICORN2 campaign of (a) W band radar reflectivity observations, (b) CAM6 COSP attenuated reflectivity as viewed from the ground, (c) AM4 COSP attenuated reflectivity as viewed from space. (d)-(f), same as (a)-(c) but for low cloud columns (maximum reflectivity above 4 km ≤ -40 dBZ). (g)-(i), same as (a)-(c) but for deep cloud columns (maximum reflectivity above 4 km ≥ -40 dBZ).

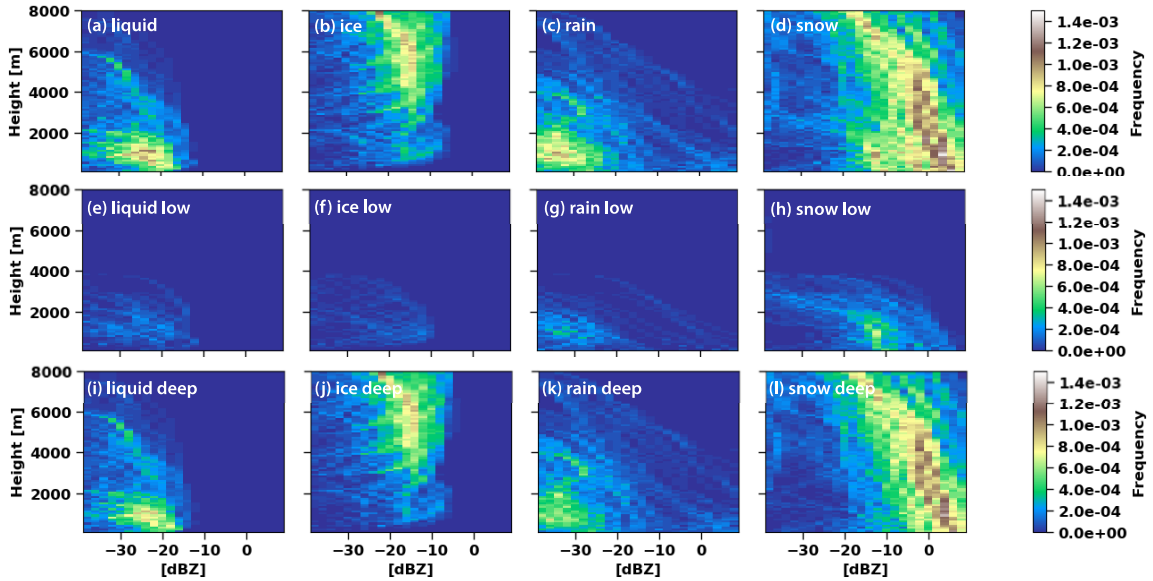

Fig. 16 CFAD for the entire CAPRICORN2 campaign of CAM6 COSP unattenuated reflectivity of (a) liquid, (b) ice, (c) rain, and (d) snow. (e)-(h), same as (a)-(d) but for low cloud columns. (i)-(l), same as (a)-(d) but for deep cloud columns.

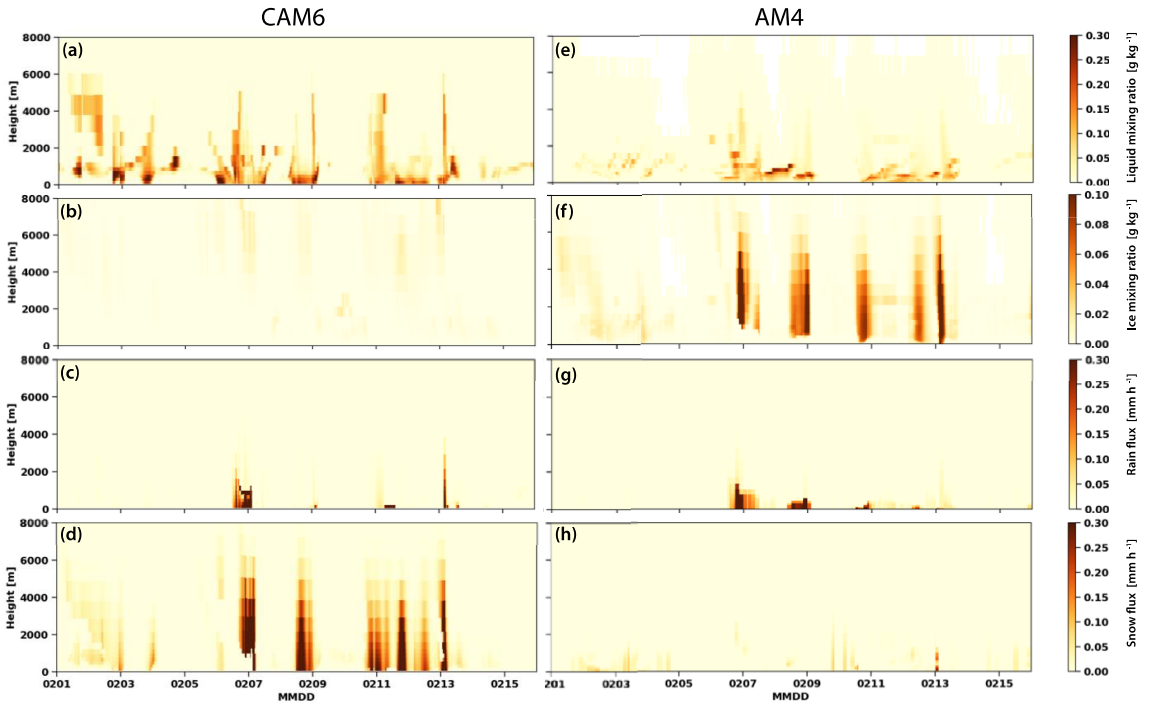

Fig. 17 (a) CAM6 liquid water mixing ratio, (b) CAM6 ice mixing ratio, (c) CAM6 rain flux, (d) CAM6 snow flux, (e) AM4 liquid water mixing ratio, (f) AM4 ice mixing ratio, (g) AM4 rain flux, and (h) AM4 snow flux during the 1-15 February 2018 period of CAPRICORN2.

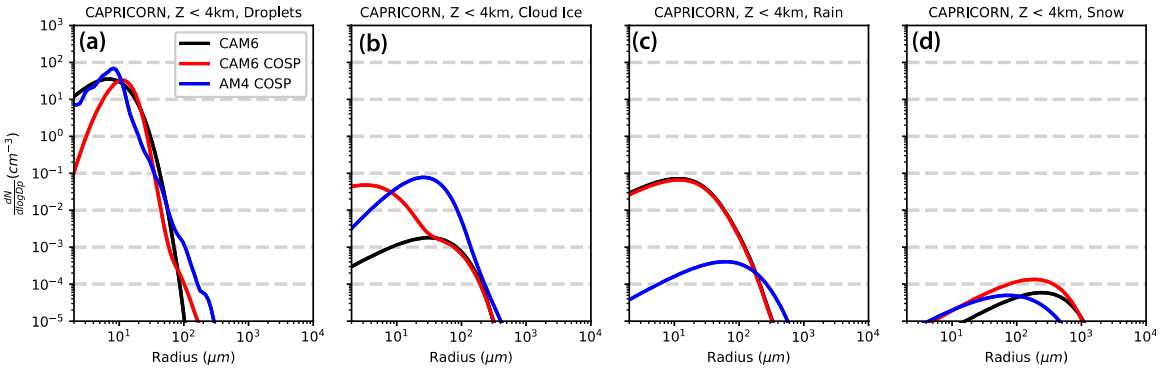

Fig. 18 Particle size distributions for low clouds in CAM6, CAM6 COSP, and AM4 COSP during CAPRICORN campaign.

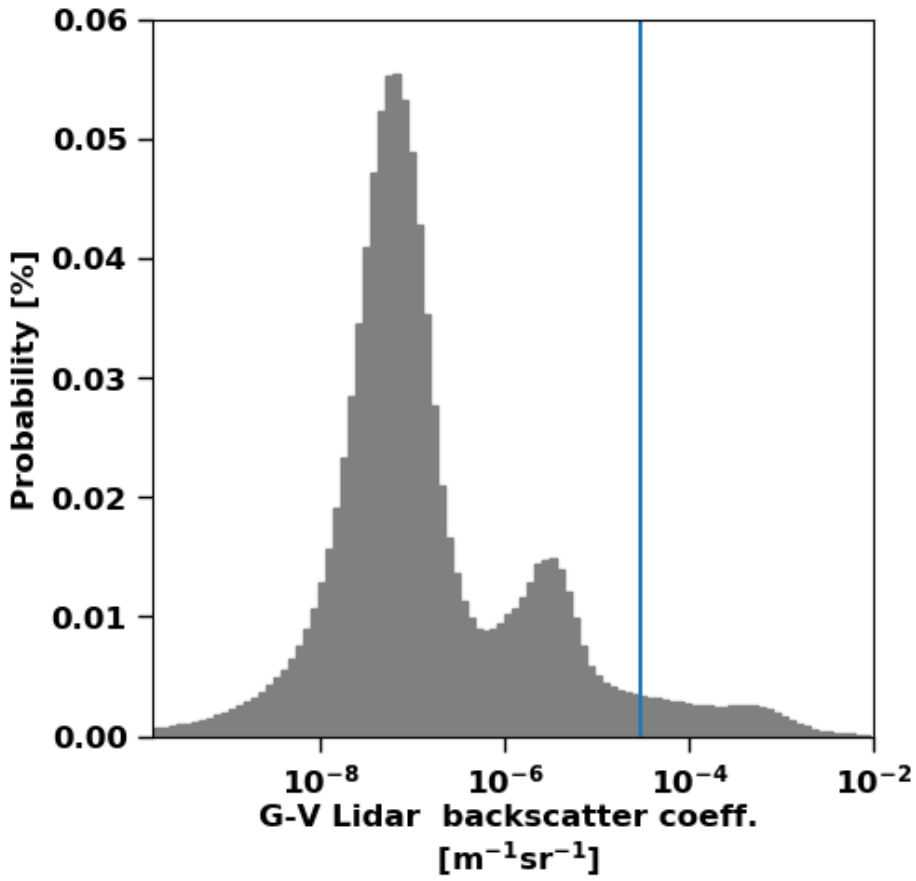

1292

1293 Fig. A1 Probability density function of HSRL backscatter coefficient for 15 flights during

1294 SOCRATES

1295

1296